

To appear in The Astronomical Journal

## DDO 43: A Prototypical Dwarf Irregular Galaxy?

Caroline E. Simpson

*Department of Physics, Florida International University, University Park, Miami, Florida  
33199 USA*

`simpsonc@galaxy.fiu.edu`

Deidre A. Hunter

*Lowell Observatory, 1400 West Mars Hill Road, Flagstaff, Arizona 86001 USA*

`dah@lowell.edu`

and

Tyler E. Nordgren

*Department of Physics, University of Redlands, 1200 East Colton Avenue, Redlands, CA  
92373 USA*

`tyler_nordgren@redlands.edu`

### ABSTRACT

We present sensitive and high resolution 21 cm observations of the dwarf irregular (dIm) galaxy DDO 43, in conjunction with optical broad and narrow band images in U, B, V, and  $H\alpha$ . The observations are used to examine the relationship between its HI morphology and kinematics to past and present star formation. Optically, it is a small ( $R_{25} = 990$  pc), faint ( $M_B$  of  $-14.0$ ) Im with a slightly boxy shape. In HI, DDO 43 has an extended ( $R_{HI}/R_H = 2.8$ ) gas envelope. There is a high density ridge associated with the optical body of the galaxy, containing several higher density knots and lower density holes. The largest hole is  $\sim 850 \times 530$  pc. No expansion is detected, so it must be relatively old. The largest and potentially oldest (7–70 Myr) of the six identified star clusters is located at the western edge of the hole. Four of the other clusters are located near high density peaks. There are several HII regions, most (but not

all) of which are associated with peaks in the H I surface density. The overall star formation rate is average for its type.

In many ways, DDO 43 is a very typical dwarf irregular galaxy. Its H I morphology is consistent with a history of episodes of localized star formation that create holes and shells in the ISM, some of which can overlap. These features are located within the area of solid-body rotation in the galaxy; the lack of shear in these small systems allows such structures to persist for long periods of time.

*Subject headings:* galaxies: irregular — galaxies: kinematics and dynamics — galaxies: ISM — galaxies: photometry — galaxies: individual: DDO 43

## 1. Introduction

DDO 43 is part of a large survey of Im galaxies being conducted by Hunter and Elmegreen (2004). The survey includes 140 Im, Sm, and Blue Compact Dwarf (BCD) galaxies, thus we can place DDO 43 in the context of a large sample. One of the purposes of the survey is to examine how star formation occurs and is regulated in low mass galaxies. The galaxies were chosen to be relatively nearby, and the sample was biased to those systems containing gas. All galaxies have been observed in H $\alpha$  and UBV, and a sub-sample in JHK and H I (neutral hydrogen). For those observed in H I, we are examining the relationship between the stellar and gaseous components of galaxies in the sample. Here we present the results for the Im galaxy DDO 43.

Optically, DDO 43 shows no hint of being different from other tiny dwarf galaxies. It looks rather rectangular in V, as many Im galaxies do, and it contains numerous H II regions. At a distance of 5.5 Mpc (determined from  $V_{GSR}$  given by de Vaucouleurs et al. 1991 [=RC3] and a Hubble constant of 65 km s<sup>-1</sup> Mpc<sup>-1</sup>), DDO 43 has an integrated  $M_B$  of  $-14.0$ . This places DDO 43 towards the faint end of the distribution of Im galaxies, but still well within normal bounds (Figure 3 of Hunter 1997). The oxygen abundance of DDO 43 was measured by Hunter & Hoffman (1999) to be  $\log O/H + 12 = 8.3 \pm 0.09$ . This value is typical of Im galaxies (see Figure 5 of Hunter & Hoffman). DDO 43 is relatively isolated. Its nearest neighbor is another Im galaxy, DDO 46, that is 270 kpc away. The nearest large galaxy is the Sc spiral NGC 2537A 1.6 Mpc away, including the radial difference.

Despite its optical normality, there were two possible characteristics of DDO 43 that led us to examine it in more detail. Our discovery of a large (galaxy-sized) hole in the H I of the dwarf Im galaxy DDO 88 (Simpson, Hunter, & Knezek 2005) prompted us to further explore DDO 43. Both DDO 88 and DDO 43 were originally observed using the Very Large

Array (VLA)<sup>1</sup> while it was in its C configuration. Although this produced data with fairly good resolution, these data suffered from low signal-to-noise, and only the highest density H I peaks in each galaxy were detected. For both DDO 88 and DDO 43, these peaks appeared to form an incomplete shell around the optical body of the galaxy (Simpson & Gottesman 2000). Intrigued by this, we obtained more sensitive H I data for both galaxies with the VLA in both C and D-configuration. These deeper images of DDO 88 revealed an extensive H I envelope, and a high-density ring of H I surrounding the bulk of the optical body (Simpson et al. 2005). The inner part of the ring is H I-deficient, and the size of the hole is comparable to the optical galaxy. There is a faint, very red cluster located approximately in the center of the hole that may be the remnant of the star-formation event that produced the H I hole.

Previous work suggests that feedback between energy deposited in the interstellar medium (ISM) by massive star formation and the ISM itself may regulate star formation in low mass dwarf galaxies. They do not possess the gravitational potentials necessary to support spiral density waves, which regulate star formation in larger galaxies, so some other mechanism must be operating. H I observations of dIrrs have revealed highly structured H I morphologies, with holes, shells, and filaments apparent (e.g. Ott et al. 2001; Stewart et al. 2000; Walter & Brinks 1999; Martin 1998; Meurer et al. 1998; Young & Lo 1996; Meurer et al. 1992; Puche et al. 1992; but see Rhode et al. 1999). Presumably, these features are both the result and cause of episodes of star formation: energy and stellar winds from massive stars sweeps up the surrounding H I producing cavities in the gas (e.g. Scalo & Chappell 1999). Denser regions of gas pile up along the boundaries, creating H I shells and filaments. Where the gas becomes dense enough, further star formation can occur.

The detection of an old, red cluster in the center of the large H I hole in DDO 88, along with the location of younger clusters in the higher density shell around the hole, is in agreement with this star formation scenario. These interesting results from our study of DDO 88 led us to examine DDO 43 to see if it also contained a large H I hole, as hinted at by the earlier VLA observations. DDO 43 is relatively similar to DDO 88 in many physical respects; has star formation had the same sort of effect on it as in DDO 88?

DDO 43 also interested us because it is listed by Hunter, Hunsberger, & Roye (2000) as a candidate old tidal dwarf galaxy. People have recently recognized that dwarf irregular (Im) galaxies can form in the tidal tails of merging spiral galaxies (Mirabel, Dottori, & Lutz 1992; Malphrus et al. 1997; Duc & Mirabel 1999). Some dwarf systems are forming this way now (Hunsberger, Charlton, & Zaritsky 1996) while others may have formed in interactions

---

<sup>1</sup>The VLA is a facility of the National Radio Astronomy Observatory, operated by Associated Universities, Inc., under cooperative agreement with the National Science Foundation.

long ago that are no longer obvious. A distinctive characteristic of tidal dwarfs is that they should have less dark matter than traditional dwarfs (Barnes & Hernquist 1992). Hunter et al. exploited this property to identify candidate old tidal dwarf systems among nearby Im galaxies. DDO 43 potentially has a maximum rotation speed that is too low for its luminosity (Simpson & Gottesman 2000; Figure 1 of Hunter et al. 2000). If borne out, this could indicate a deficit of dark matter and make DDO 43 a strong candidate for a tidal dwarf.

## 2. Data Acquisition and Reductions

### 2.1. Optical

We used the Hall 1.1 m telescope at Lowell Observatory to obtain B and V images of DDO 43 1999 February and U images 1999 November. We used a SITe 2048×2048 CCD binned  $2 \times 2$ . The exposure times were  $6 \times 900$  s for V,  $5 \times 1800$  s for B, and  $3 \times 1800$  s for U. The pixel scale was  $1.13''$ , and the seeing in the final averaged images was  $2.9''$  in V,  $2.3''$  in B, and  $2.6''$  in U. The electronic pedestal was subtracted using the overscan strip, and the images were flat-fielded using sky flats. Landolt (1992) standard stars were used to calibrate the photometry. The images in each filter were averaged with an algorithm to reject cosmic rays while still preserving the photometric integrity of the image.

Before performing surface photometry, we edited foreground stars and background galaxies from the final UBV images. The V-band image was done by hand, and then the cursor log file produced from that was used to remove objects from the other two filters. In that way, stars were removed in the same way for each filter. We then made a two-dimensional fit to the background and subtracted it from the image to produce a sky-subtracted final image for analysis.

We obtained  $H\alpha$  images of DDO 43 in 1995 February with the Perkins 1.8 m telescope at Lowell Observatory. We used a TI  $800 \times 800$  CCD provided to Lowell Observatory by the National Science Foundation and the Ohio State University Fabry-Perot as a 3:1 focal reducer. The  $H\alpha$  filter has a central wavelength of  $6566 \text{ \AA}$  and a FWHM of  $32 \text{ \AA}$ . The contribution from stellar continuum was determined using an off-band filter centered at  $6440 \text{ \AA}$  with a FWHM of  $95 \text{ \AA}$ . The off-band image was shifted, scaled, and subtracted from the  $H\alpha$  image to remove the stellar continuum and leave only  $H\alpha$  nebular emission. The  $H\alpha$  observations consisted of three 3000 s images, preceded by a 900 s off-band observation. The pixel scale was  $0.49''$ , and the stellar FWHM on the final image is  $1.6''$ . The electronic pedestal was subtracted using the overscan strip, and the images were flat-fielded using

observations of a white spot hanging on the inside of the dome.

The  $H\alpha$  flux was calibrated using observations of the NGC 2363 nebula (Kennicutt, Balick, & Heckman 1980). The  $H\alpha$  flux has been corrected for the shift of the bandpass with temperature and for contamination by the  $[NII]\lambda 6584$  emission line in the bandpass (a 1% correction).

## 2.2. H I Data

21 cm spectral line observations of DDO 43 were made using both the D and C configurations of the VLA. Time on source for both observations was approximately 4.5 hours. The D configuration, which is the VLA’s most compact, provides short spacings, resulting in high sensitivity but at the cost of spatial resolution: the synthesized beam is on the order of  $1'$ . The C configuration, with longer baselines, provides higher resolution (nominally  $12.5''$ ) but lower sensitivity. Observations for both configurations were made using a 128 channel spectrometer in 2IF mode with on-line Hanning smoothing. This results in a channel separation of 12.2 kHz ( $2.6 \text{ km s}^{-1}$ ) for a total observed bandwidth of 1.56 MHz. For spectral line data that are taken using on-line Hanning smoothing, the velocity resolution is equal to the channel separation, and so is also  $2.6 \text{ km s}^{-1}$ .

Observations of the nearby continuum source 0713+438 (J2000) were made for phase calibration of both data sets; observations of the sources 0137+331 (J2000) and 1331+305 (J2000) were made for calibration of the flux and bandpass of the C and D-configuration data, respectively. Calibration of both data sets was performed using the standard routines in AIPS. Observational information is provided in Table 1.

The D-configuration source data were affected by solar contamination on the short baselines. The corrupted data were flagged, removing approximately 8% of the total number of visibilities. There were three strong continuum sources in the field; there was no sign of continuum emission from DDO 43. The continuum was satisfactorily subtracted in the  $uv$  plane by using line-free channels to make a linear fit to the continuum emission. The resulting continuum-free data was then imaged using the AIPS task IMAGR. To ensure the best sensitivity to low levels of emission, natural weighting was used. The data were CLEANed during imaging to reduce the sidelobes produced by non-gaussian features in the “dirty” beam. No clean boxes were specified, so the default of a box ten pixels smaller than the image size was used. No zero-spacing flux was assumed. The specified flux cutoff of 0.83 mJy/B ( $\sim 1\sigma$  in a single channel) was reached in less than 3000 iterations in each channel, which is less than the 10,000 iteration cutoff set in the task.

The resulting data cube (one channel for each observed frequency) has a beam size of  $54.8'' \times 53.7''$  and a single channel r.m.s. of 0.81 mJy/B. Line emission appears from approximately 300–420 km s<sup>-1</sup>. The data cube was integrated in velocity with the task MOMNT to produce moment maps of the integrated flux density, the flux-weighted velocity field, and the velocity dispersions. The integration task first smooths the data spatially and then in velocity space to create a lower-noise mask. A cutoff of approximately 1.5 times the single-channel r.m.s. was applied to the mask, and pixels in the original, unsmoothed cube corresponding to the mask pixels higher than the cutoff flux were integrated.

The C-configuration data were very well behaved resulting in minimal data editing. No solar contamination was present, but like the D configuration, there were still the three strong continuum sources. This continuum emission was subtracted as for the D-configuration data. The imaging was done using uniform weighting (ROBUST = 1) however, to produce high resolution images with only a slight degradation in sensitivity. This resulted in a beam size of  $14.0'' \times 11.0''$  and a single-channel r.m.s. of 1.05 mJy/B. As for the D-configuration data, the data were CLEANed during imaging. In this case, a test showed that the CLEAN component flux leveled off after the first 500 iterations, and so an iteration cutoff of 2500 was used in conjunction with a flux cutoff of 0.6 mJy/B ( $\sim 0.5\sigma$ ). The same defaults of no zero-spacing flux and no specified CLEAN boxes were used. After imaging, the cube was integrated in velocity using a flux cutoff of  $1.5\sigma$  to produce moment maps as was done for the D-configuration data.

Once the C and D-configuration data were calibrated, they were combined in the  $uv$  plane to produce a data set with both good resolution and sensitivity. This combined C+D dataset was imaged using both natural (C+D<sub>NA</sub>) and uniform (C+D<sub>UN</sub>; ROBUST = 1) weighting. The naturally-weighted data cube has a beam size of  $24.5'' \times 17.1''$  and a single-channel r.m.s. of 1.05 mJy/B. The uniformly-weighted cube has a beam size of  $20.30'' \times 14.00''$  and a single-channel r.m.s. of 1.07 mJy/B (see Table 1). As for the C configuration data, an iteration cutoff of 2500 was determined to be adequate, and was combined with a flux cutoff of 0.6 mJy/B ( $\sim .5\sigma$ ) for the uniform weighted data. For the naturally weighted data, the iteration limit was set to 3500. No clean boxes or zero-spacing flux were specified.

In Figure 1 we show the velocity profiles from our C+D-configuration data (natural weighting) and from single-dish data from the Effelsberg 100 m radio telescope (Huchtmeier & Richter 1986). From our D-configuration data, we find an integrated source flux of 12.9 Jy km s<sup>-1</sup>, which is similar to three of the four single-dish flux measurements listed in the Huchtmeier & Richter catalog (1989). The fourth measurement, the one from the Effelsberg 100 m radio telescope, is quite a bit higher at 16.9 Jy km s<sup>-1</sup>. The Effelsberg beam at 21

cm is  $9'$ ; a search within a  $9'$  radius of DDO 43 using NED<sup>2</sup> turned up only a few continuum sources, so it is unlikely that this discrepancy in the measured flux is caused by confusion in the Effelsberg beam.

If the Effelsberg flux is correct, we have only recovered 76% of the H I flux. We have checked our flux calibration by comparing the catalogued flux densities of two (unresolved) continuum sources in the field with the fluxes measured from our data. These sources are within  $3$ – $4'$  of DDO 43; they are catalogued in the NRAO VLA Sky Survey (NVSS<sup>3</sup>; Condon et al. 1998). In the C-configuration data, our measured fluxes (44.6 and 94.1 mJy) are an average of 7% lower than the NVSS values of 48.9 and 97.9 mJy; for the D-configuration (42.4 and 88.6 mJy) they are 12% lower. If we assume this is accurate and correct our integrated flux for DDO 43 by 12% for the D-configuration data, we are still only detecting 85% of the reported Effelsberg value.

Another possibility is that the VLA interferometer is missing some of the flux detected by the Effelsberg single-dish instrument. Interferometers are “blind” to structures larger than an angular size that depends on the projected baseline lengths between the antennas. The D configuration can detect structures up to  $15'$  across per spectral channel before they are resolved out by the interferometer. If the discrepancy is due to a low-level envelope too large to be detected by the VLA, it would have to be approximately twice the extent of the H I that we detected (see §3.2 below). This seems unlikely, as does missing faint emission with our sensitive observations. As our estimate agrees with the other three catalogued measurements, it would seem that the Effelsberg value is suspect.

### 3. Results

#### 3.1. Optical

##### 3.1.1. Morphology

The logarithm of our V-band image of DDO 43 is shown in the left panel of Figure 2. The most striking feature of the image is the rather rectangular morphology of the middle isophotes. This morphology resembles, for example, that of the Im galaxies DDO 75, NGC 1156, NGC 2366, and NGC 4449. This shape suggests the presence of a stellar bar potential. The identification of bars in Im galaxies is complicated by the lack of symmetry provided by

---

<sup>2</sup>NASA/IPAC Extragalactic Database; <http://nedwww.ipac.caltech.edu/>

<sup>3</sup><http://www.cv.nrao.edu/nvss/>

spiral arms and is especially difficult if the bar is comparable in size to the galaxy (Roye & Hunter 2000). However, there are some properties that can offer additional evidence that a bar is present.

First, we fit the rectangular part of the V-band isophotes with a curve of the form  $(\frac{|x|}{a})^c + (\frac{|y|}{b})^c = 1$ , where  $a$  and  $b$  are the semi-major and minor axes and  $c$  is a parameter that describes the boxiness of the bar structure (Athanasoula et al. 1990). For  $c = 2$  the structure is an ellipse, for  $c < 2$  the structure is “disky,” and for  $c > 2$  the structure is “boxy.” The best fit for DDO 43 is a curve with  $c = 3$ , a boxy structure centered at  $7^h 28^m 17.55^s$ ,  $40^\circ 46' 09.8''$  (J2000) with a bar semi-major axis  $a_{bar}$  of  $33''$  at a position angle of  $20^\circ$ . This curve is shown in Figure 2 superposed on the logarithm of the V-band image. The Im galaxies NGC 2366 and NGC 4449 are also best fit with a  $c = 3$  boxy curve (Hunter, Elmegreen, & van Woerden 2001; Hunter, van Woerden, & Gallagher 1999). Fitting a boxy elliptical does not require that a bar be present (see discussion of NGC 2366, Hunter et al. 2001), but it does suggest that one could be present.

A second observational clue to the presence of a bar can be the twisting of isophotes as one goes from the bar to the disk. This is clearly seen in NGC 4449, for example (Hunter et al. 1999), but is not a necessary condition. In DDO 43 there is a small shift in the position angle of the major axis as one goes from the inner isophotes fit with the boxy curve ( $\mu_{V_0} = 24.4 \text{ mag arcsec}^{-2}$ ) to outer isophotes. The inner rectangle is best fit with a boxy curve with a position angle of  $20^\circ$  while the outer isophotes have a position angle of  $6.5^\circ$ . This is a shift of  $13.5^\circ$  and it is clearly visible in Figure 2.

A third characteristic of a bar is a potential mis-alignment between the kinematic line of nodes and the major axis of the bar. In a barred galaxy, the isophotes are not circular in the principal plane, and the stellar orbits may precess, so the line of nodes and morphological axis need not be aligned. This is the case in, for example, NGC 1156 (Hunter et al. 2002). We will discuss the gas kinematics in DDO 43 below, but it is appropriate to mention here that the position angle of the line of nodes of the rotating gas system is  $294^\circ$ . Thus, the kinematic line of nodes and the major axis of the rectangular part of the galaxy are nearly perpendicular, being mis-aligned by  $86^\circ$ . This is strong evidence that the boxy appearance of the optical galaxy is in fact due to a stellar bar potential.

However, if DDO 43 is barred, the bar occupies a large fraction of the optical galaxy. This is also the case in NGC 1156, NGC 2366, and NGC 4449. In DDO 43  $a_{bar}/R_{25}$  is 0.8; where  $R_{25}$  is the radius at a  $\mu_{B_0}$  of 25 magnitudes per  $\text{arcsec}^{-2}$ . In NGC 2366 this ratio is 1.6 and in NGC 4449 it is 0.6. By contrast, in Sd–Sm spiral galaxies  $a_{bar}/R_{25}$  is 0.05–0.3 (Elmegreen & Elmegreen 1985, Martin 1995, Elmegreen et al. 1996). Thus, DDO 43 and other barred Im galaxies are unusual in being dominated optically by the bar if it is present.



In Figure 3 we show surface brightness cuts in V along the major and minor axis of the bar. The cuts are 20'' wide. The cuts from DDO 43 are more rounded at the top than cuts across the bar of NGC 4449, but resemble similar cuts made in NGC 2366. The surface brightness of bars in late-type spirals are more often fit with an exponential whereas those in early-type spirals are flatter (Combes & Elmegreen 1993, Elmegreen et al. 1996). The profiles of DDO 43 resemble those of a few Scd–Sm galaxies with exponential profiles shown by Elmegreen et al. (1996).

### 3.1.2. Broad-band Surface Photometry

We present UBV surface photometry in Figure 4. To measure the surface photometry we used ellipses with a position angle of 6.5°, a ratio of minor to major axis ratio  $b/a$  of 0.70, and a semi-major axis step size of 11.3''. The  $b/a$ , position angle, and center were determined from an outer isophote on a  $2 \times 2$  block-averaged version of the V-band image. The surface photometry and colors have been corrected for reddening using a total  $E(B-V)_t = E(B-V)_f + 0.05$ , where the foreground reddening  $E(B-V)_f$  is 0.055 (Burstein & Heiles 1984) and we add 0.05 for nominal internal reddening. We use the reddening law of Cardelli, Clayton, & Mathis (1989) and  $A_V/E(B-V) = 3.1$ . Thus,  $A_V$  is 0.33 and  $E(U-B)$  is 0.07.

From the reddening-corrected B-band surface photometry  $\mu_{B_0}$  we measure  $R_{25}$  to be 37'', which is 990 pc at the galaxy. Our radius is 7% smaller than that given by RC3. The Holmberg radius,  $R_H$ , originally defined to a photographic surface brightness, is measured at an equivalent B-band surface brightness  $\mu_B = 26.7 - 0.149(B - V)$ . For a  $(B-V)_0$  of 0.32, the Holmberg radius is determined at a  $\mu_{B_0}$  of 26.65 magnitudes of one arcsec<sup>-2</sup>. We find an  $R_H$  of 53'', which is 1.4 kpc at the galaxy. Integrated properties of DDO 43 are listed in Table 2.

We fit an exponential disk to  $\mu_{V_0}$ , and the fit is shown in Figure 4. DDO 43 is fit well with an exponential disk profile having a central surface brightness  $\mu_0$  of  $22.4 \pm 0.2$  magnitudes of one arcsec<sup>-2</sup> and a disk scale length  $R_D$  of  $430 \pm 50$  pc. Both these values are normal for Im galaxies (Hunter & Elmegreen 2004, de Jong 1996).

DDO 43's integrated colors are typical of Im galaxies (see Figure 2 of Hunter 1997). Integrated values are given in Table 2, and annular colors are shown in Figure 4. As in most irregulars, the colors are, within the uncertainties, constant with radius. Two-dimensional color ratio images further substantiate that there is no large-scale pattern to the colors.

### 3.1.3. *Star-formation Activity*

We show our H $\alpha$  image of DDO 43 in the right panel of Figure 2. There one can see that DDO 43 contains numerous H II regions scattered across the disk of the galaxy. The most distant H II region from the center of the galaxy is found in the northern part of the galaxy just beyond the Holmberg radius at 1.5 kpc, which is not unusual (see Figure 15 of Hunter & Elmegreen 2004). The largest H II region, in the eastern part of the galaxy, has an H $\alpha$  luminosity of  $1.0 \times 10^{38}$  ergs s $^{-1}$ , which is equivalent to 10 Orion nebulae (Kennicutt 1984). Thus, the H II regions in DDO 43 are quite modest in size.

The azimuthally-averaged H $\alpha$  surface brightness is shown with the UBV surface photometry in Figure 4. The V-band surface photometry and H $\alpha$  surface photometry are displayed so that they cover the same logarithmic interval and, thus, the slopes of the profiles can be directly compared. We see that, although star formation is found in the center of the galaxy, the surface density is less than would be expected. As a result, there is a depression in the star formation activity in the central 0.75 kpc of the galaxy. Beyond there the star formation activity drops off in step with the drop in stellar surface density, as is common in Im galaxies (Hunter, Elmegreen, & Baker 1998, Hunter & Elmegreen 2004).

The H $\alpha$  luminosity and derived star formation rate of the galaxy are given in Table 2. DDO 43 has a star formation rate per unit area that is in the middle of the range seen in Im galaxies (see Figure 9 of Hunter & Elmegreen 2004). At its current rate of consumption, the galaxy can turn gas into stars for another 25 Gyr if all of the gas associated with the galaxy can be used. The timescale to run out of gas is even longer if recycling of gas from dying stars is efficient. This timescale to exhaust the gas is typical of Im galaxies (Hunter & Elmegreen 2004), and the galaxy can continue forming stars at its current rate for several more Hubble times.

### 3.1.4. *Star Clusters*

The V-band image of DDO 43 clearly shows knots that appear to be star clusters. These are numbered in Figure 2. We measured the UBV photometry of these clusters through apertures that just included the cluster as seen on the V-band image, radii of 1.7'' to 4.0''. To determine the contribution to the signal from the underlying galaxy, we used an annulus 4.0–6.2''. The cluster photometry is listed in Table 3 and shown in Figure 5 along with the cluster evolutionary track of Leitherer et al. (1999) for a metallicity of  $Z = 0.008$ . The evolutionary track is used to determine the allowed ages of the clusters. The uncertainties of the colors allow a range of ages in most cases. However, clusters 3–6 are associated with

H $\alpha$  nebular emission, so the younger end of the range of allowed ages is more likely for these clusters.

Because star clusters fade and redden as they evolve, to compare the photometry of clusters requires that one refer them to a common age. We use the fiducial age of 10 Myrs adopted by Billett, Hunter, & Elmegreen (2002). The  $M_V$  that the DDO 43 clusters would have at an age of 10 Myrs ( $M_V(10 \text{ Myr})$ ) are given in Table 3. We can then use  $M_V(10 \text{ Myr})$  as a way to indirectly compare the masses of the clusters. We adopt the quantitative definitions of “populous” and “super” star clusters initiated by Billett et al.:  $M_V(10 \text{ Myr}) \leq -10.5$  for a super star cluster and  $-9.5 \leq M_V(10 \text{ Myr}) < -10.5$  for a populous cluster. Super star clusters are the most luminous and massive clusters; populous clusters are less so but still substantial. Only cluster 1 in DDO 43 could be as luminous as a populous cluster if it is as old as the upper end of its range of allowed ages. Since nebular emission is associated with cluster 4, the lower age and hence lower  $M_V(10 \text{ Myr})$  is more likely, and so cluster 4 is not likely a populous cluster. Clusters 2–6 are relatively small.

## 3.2. H I

### 3.2.1. Morphology

The naturally-weighted C+D channel maps are shown in Figure 6. There is emission in the velocity range from approximately 325 km s $^{-1}$  to 385 km s $^{-1}$ . Rotation is present, but primarily solid-body, which is not unusual for dwarf galaxies (Swaters 1999). The H I distribution appears clumpy, with high density knots embedded in the more dense regions of the galaxy.

The D-configuration alone, with its short baselines and resulting large beamsizes ( $54.8'' \times 52.7''$ ), is unable to resolve any clear structure in the H I of the galaxy. It does however recover the most flux and is more sensitive to any large scale structures that may be present. The integrated flux map from the D-configuration data shows only a relatively circular distribution with the flux density increasing fairly smoothly towards the center of the galaxy. A total of  $9.2 \times 10^7 M_\odot$  of H I is detected. The H I extends far beyond the optical body of the galaxy (Figure 7). The H I radius at the  $5 \times 10^{19} \text{ cm}^{-2}$  contour is 146'' (3.9 kpc; corrected for the beam-size), which is 2.8  $R_H$ . This is a large ratio, as indicated by those measured for Sextans A (1.3, Skillman et al. 1988), DDO 50 (1.5, Puche et al. 1992), and DDO 155 (1.9, Carignan et al. 1990); and by comparison to the sample plotted in Figure 13 of Hunter 1997. Although the sample in Hunter 1997 uses the radii at  $1 \times 10^{19} \text{ cm}^{-2}$ , DDO 43’s ratio using the smaller  $5 \times 10^{19} \text{ cm}^{-2}$  contour still falls above the median. This is also reflected in

its high HI mass-to-light ratio of 1.64. Although optically DDO 43 is about a magnitude fainter and about one-half the size of DDO 88, it has a larger HI mass and radius than DDO 88. HI properties are listed in Table 2.

In Figure 8 we show the integrated HI flux density from the naturally-weighted C+D data. For comparison, the C+D-configuration flux contours are shown on the D-configuration flux map in Figure 9. Note that a larger region ( $8' \times 8'$ ) is plotted for both this figure and Figure 7 than for the others ( $5' \times 5'$ ). This is necessary to show the full extent of the HI distribution mapped by the D configuration. From this, we can see that the extensive low-level HI envelope seen in the D-configuration map is not detected in the C+D<sub>NA</sub> map. The HI in the C+D<sub>NA</sub> map can only be measured out to  $N_{HI} = 5 \times 10^{19} \text{ cm}^{-2}$ , which is at a radius of  $115''$  (3.1 kpc). Although this extends to only 63% of the total D-configuration radius, it contains 94% of the total HI mass measured from the D-configuration data. Only 6% is in the outer envelope, so it is indeed tenuous.

Although lacking the D configuration’s sensitivity, the higher spatial resolution of the C+D<sub>NA</sub> data (FWHM =  $24.5'' \times 17.1''$ ), begins to show some structure in the HI. There is a small depression or hole in the gas just south of the galaxy center, with a very high density knot of HI just south of the depression. There are three more dense regions just north of the center. The outer contour is not symmetrical; there is a faint, slightly extended area of emission on the west side of the HI distribution. The average column density in this extended region is  $\sim 1.1 \times 10^{20} \text{ cm}^{-2}$  and the peak column density is  $2.8 \times 10^{20} \text{ cm}^{-2}$ .

To examine the small-scale structure features in the HI distribution more clearly and at the highest resolution, we produced an integrated flux map based only on the C-configuration data cube using uniform weighting (beam size  $14.0'' \times 11.0'' = 370 \times 290 \text{ pc}$ ). Without the larger number of short baselines provided by the D-configuration, the fainter, larger-scale structures are not mapped, making it easier to identify the (brighter) small-scale structures. Not all the information provided by short baselines is lost however, as the version of the C-configuration that was used for the observations has the same minimum spacing as the D-configuration. (This C-configuration, now standard, was originally known as CS, and has an antenna from the north arm moved to the central antenna pad).

The uniformly-weighted flux map from the C-configuration data more clearly reveals the high density knots and low density holes in the HI in the inner region of the galaxy (Figure 10). The large hole south of center is well-defined in this image, and a second depression is visible just northwest of center. All these features are located within the  $N_{HI} \geq 1 \times 10^{21} \text{ cm}^{-2}$  contour, which extends  $76''$  (2.0 kpc) in RA and  $100''$  (2.7 kpc) in DEC. The mass of the HI inside this high density contour is  $4.0 \times 10^7 M_{\odot}$ , which is 44% of the total HI mass of the galaxy.

We have defined “knots” as regions with column densities higher than  $1.2 \times 10^{21} \text{ cm}^{-2}$  in the C-configuration map. There are six knots using this criterion; only the brightest and largest (Knot 1), located in the south of the galaxy, is somewhat resolved. It is approximately  $750 \times 430 \text{ pc}$  in size. The average column density of the knots is  $\sim 1.3 \times 10^{21} \text{ cm}^{-2}$ , with a peak column density of  $1.48 \times 10^{21} \text{ cm}^{-2}$  located in Knot 1. The combined H I mass of the knots is  $\sim 8 \times 10^6 M_{\odot}$ , which is 21% of the H I mass contained within the high density region and 9% of the total H I mass.

“Holes” are defined as areas with column densities less than  $1 \times 10^{21} \text{ cm}^{-2}$  that are located inside the high density region delineated by the  $N_{HI} > 1 \times 10^{21} \text{ cm}^{-2}$  contour. There are four of these areas: the large, well-defined hole in the south, two smaller overlapping holes just northwest of center, and a very small depression to the northeast of that. Only the large hole is resolved; it is roughly  $850 \times 530 \text{ pc}$  across, making it larger than Knot 1 just south of it. The average column density in this hole is  $7.8 \times 10^{20} \text{ cm}^{-2}$ .

The C-configuration flux density contours are shown on the V image in Figure 11. The higher density H I knots are located in the outskirts of the optical body of the galaxy, but the high density region also extends across the center of the bright optical emission in the galaxy. The northern edge of the large H I hole just overlaps the southern part of the bright optical region.

Of the five star clusters seen on the V image, four are located at the edges of the high density knots; one (Cluster 1; the largest) is located just within the western edge of the large hole and another (Cluster 2) is between the hole and the large H I knot. These clusters are potentially the two oldest, based on evolutionary models and the lack of any surrounding H $\alpha$  nebula.

### 3.2.2. HI Surface Density

In Figure 12 we show the azimuthally-averaged surface density of the H I gas in DDO 43. We have integrated the H I in  $20''$  radial steps using the naturally-weighted C+D-configuration map (beam size  $24.5'' \times 17.1''$ ). We used the center ( $7^h 28^m 17.2^s$ ,  $40^{\circ} 46' 15.2''$ ; J2000), position angle ( $294^{\circ}$ ), and inclination ( $i = 42^{\circ}$ ) found from determining the rotation curve, discussed below. We have multiplied the H I surface density by 1.34 to include He.

In Figure 12 we have also plotted several other Im galaxies, selecting those for which the beam size is comparable to that of DDO 43. The DDO 43 map had a beam of  $650 \times 460 \text{ pc}$ ; NGC 2366’s is  $560 \times 480 \text{ pc}$  (Hunter et al. 2001); DDO 75’s is  $530 \times 440 \text{ pc}$  (Wilcots &

Hunter 2002); and DDO 88’s is  $600 \times 520$  pc (Simpson et al. 2005). We also include NGC 4449, although it was mapped with a smaller beam ( $185 \times 150$  pc), as an example of a system with large extended filamentary structure in the outer H I envelope (Hunter et al. 1999).

We see that averaged in  $20''$ -wide annuli, the gas surface density in DDO 43 drops off smoothly with an outer H I envelope that drops off fairly slowly. Except for the central peak in NGC 2366, DDO 43’s H I surface density profile most closely resembles that of NGC 2366.

### 3.2.3. Kinematics

#### *Rotation*

The H I velocity field of DDO 43 is shown in Figure 13 as contours superposed on the integrated H I map of the galaxy. One can see that there is overall rotation with the northwest part of the galaxy receding and the southeast part approaching. Superposed on this rotation, however, is a complex S-distortion that sets in beyond a radius of about  $60''$ . The first kinks in the isovelocity contours approximately coincide with the H I ridge in the northern part of the inner galaxy and the large H I complex in the southern part of the galaxy. An S-distortion is usually the signature of a warp in the outer parts of the H I disk. In fact, the velocity field of DDO 43 resembles that of M83, especially on the approaching side. M83’s velocity field has been fit with tilted rings that vary in position angle and inclination (Rogstad, Lockhart, & Wright 1974).

Another view of the velocity field can be obtained from a position-velocity plot. We have made a  $20''$  cut through the velocity field of the C+D<sub>UN</sub> cube at a position angle of  $294^\circ$ , the kinematic line of nodes that we find below. That position-velocity diagram is shown in Figure 14. One can see there and in Figure 13 that the rotation levels off and may turn over in the outer parts.

We fit the velocity field determined from the natural-weighted C+D-configuration maps with tilted rings using the task GAL in AIPS. The beam size in this map is  $24.5'' \times 17.1''$ , so we used  $20''$  wide rings stepped every  $20''$ . We began by fitting the entire velocity field, the approaching side only, and the receding side only and allowing all parameters to vary. Generally speaking the approaching side was harder to fit than the receding side or both halves together.

We found that the center and systemic velocity were quite stable from ring to ring and among the three solutions, so we determined the average from the solution to the entire field and fixed those parameters. The kinematic center is  $7^h 28^m 17.2^s \pm 0.4^s$ ,  $40^\circ 46' 15.2'' \pm 4.4''$

(J2000), and is marked as the large X in Figure 13. The kinematic center is  $-0.35^s$ ,  $+5.4''$  from the center of the optical bar (§3.1.1). The systemic velocity was found to be  $355 \pm 1 \text{ km s}^{-1}$ . This is the same as values found by Simpson & Gottesman (2000;  $356 \pm 0.4 \text{ km s}^{-1}$ ) from VLA observations and by Stil & Israel (2002;  $355 \pm 1 \text{ km s}^{-1}$ ) from WSRT observations. We then fixed the center and systemic velocity and fit the velocity field again. The variation of the position angle with radius and among the three velocity field fits was small, so we fixed the position angle at  $294 \pm 3^\circ$ . This value for the position angle is the same as that found by Stil & Israel ( $296 \pm 4^\circ$ ), and it is  $86^\circ$  different from the position angle of the optical bar. The average position angle is shown as the solid straight line in Figure 13, and the variation with radius is shown in the middle panel of Figure 15. We then fixed the position angle and refit the velocity field.

The variations in the inclination with the center, systemic velocity, and position angle fixed are fairly small. However, if a warp is present, the inclination need not be the same throughout the disk. Therefore, we adopted an average inclination of  $42 \pm 5^\circ$  for the disk interior to a radius of  $60''$ , where the S-distortion becomes visible in Figure 13. Beyond  $60''$ , the inclination determined for each ring was used in determining the final rotation speed at that radius. The variation of inclination with radius is shown in the bottom panel of Figure 15, and the final rotation curve is shown in the top panel. We show the rotation curve for fits to the receding and approaching halves separately and for the fit to the entire velocity field.

The rotation curve in Figure 15 is relatively normal. It rises rapidly in the center and begins to gently turn over around a radius of  $30''$  (800 pc). By  $60''$  the rotation speed appears to level off. At a radius of  $110''$  (2.93 kpc) there is an abrupt rise to a higher rotation speed in the approaching half of the galaxy clearly caused by a corresponding drop in the inclination angle. Otherwise, the rotation curve of the receding half drops in the outer parts. The maximum rotation speed, leaving out the bump at  $110''$ , occurs around a radius of  $70''$  (1.87 kpc) at a speed of  $25 \text{ km s}^{-1}$ . Stil & Israel (2002) give a rotation speed  $V \sin i$  of  $17.5 \pm 3.9 \text{ km s}^{-1}$  at a radius of  $90''$  for DDO 43. At that radius our  $V \sin i$  would be the same at  $17.6 \pm 0.8 \text{ km s}^{-1}$ .

To examine the quality of the fit, we made a model of the velocity field, then subtracted it from the observed velocity field. The residual map is shown in Figure 16. The values of the residuals range from  $-6.6$  to  $7.1 \text{ km s}^{-1}$ , so in general, the fit seems quite good. We have plotted contours from the model velocity field on the residual map in Figure 17 and the observed velocity field contours on the residual map in Figure 18. The model successfully recreates the weak turnover in each side of the velocity field, but the residual map shows that it had difficulty with the receding half turnover in the sense that it underestimates it

and shifts it slightly north. There is another region of higher-than-average residuals just south of the center of the galaxy; this area slightly overlaps the west sides of the large hole and knot in the HI. This is also near the region of highest velocity dispersion in the galaxy, so perhaps it is not surprising that the velocity residuals are larger here as well. From Figure 18, it can be seen that most of the regions of larger residuals (especially negative residuals) coincide with the kinks in the isovels that may be representative of a warp. The residuals are still small however, indicating that it's not a significant warp.

The original listing of DDO 43 as a candidate tidal dwarf by Hunter et al. (2000) was based on a suggested rotation speed of order  $9 \text{ km s}^{-1}$ . As a result, on a plot of  $M_B$  versus the maximum rotation speed (Figure 1 of Hunter et al.) DDO 43 stood out as unusually luminous for its rotation speed. This could imply a deficit of dark matter, a characteristic of tidal dwarfs (Barnes & Hernquist 1992). However, with a maximum rotation speed of  $25 \text{ km s}^{-1}$ , found here, DDO 43 now lies close to the mean of the relationship defined by other Im galaxies and spirals in that plot. Thus, DDO 43 is unlikely to be without dark matter, and unlikely to be a tidal dwarf. This is comforting since there was no obvious nearby post-merger object to have been the parent of DDO 43 if it were a tidal dwarf.

### *Velocity Dispersion*

A grey-scale display of the velocity dispersion map from the C+D<sub>NA</sub> data is shown in Figure 19 with contours of the integrated HI superposed. Within the optical body of the galaxy, the velocity dispersion is around  $10 \text{ km s}^{-1}$ . This is the value found in most quiescent gas disks. There are a few spots with higher values up to about  $12 \text{ km s}^{-1}$ , most notably the large hole. The high column density region is fairly well demarcated by the  $8 \text{ km s}^{-1}$  contour. Outside of the optical galaxy the velocity dispersion drops, and values in the extended gas are of order  $5 \text{ km s}^{-1}$ . Thus, the velocity dispersions in the HI in DDO 43 appear to be quite normal.

However, the second moment map of the galaxy does not tell the whole story. To better examine the kinematics in the HI knots and holes, using the C+D<sub>UN</sub> cube we plotted the spectra of pixels (averaged across a beamwidth) for several of the knots and the large hole. The spectra of the knots are complex. Many exhibit a central double peak, often with smaller peaks, sometimes on both sides of the bright peak, sometimes only visible as broad wings on one or both sides.

We fit gaussians to the Hanning-smoothed beam-averaged spectra of the brightest knot and the large hole; the spectra are shown in Figure 20. For the knot, we were able to successfully fit three components to 19 of the 28 spectra and two components to six spectra.



Three spectra had large uncertainties to the fits and so were not included in our analysis. For the 19 spectra with good fits to three components, the average difference in velocity between the central and two side components is  $\sim \pm 15 \text{ km s}^{-1}$ . The average amplitudes are 2, 11, and 4 mJy/B going from high to low velocity. The central and low velocity components are broad, with an average width of  $\sim 17 \text{ km s}^{-1}$ . The high velocity component is narrower, with an average width of roughly half that.

The beam-averaged spectra of the large hole are more complex than those of the knots, with most being fit by four components. Three of the 18 spectra were fit with three components, and one was fit with two. Labelling the components 1–4 from high to low central velocities, components 1 and 3 have average widths of approximately  $10 \text{ km s}^{-1}$ , while components 2 and 4 have average widths of around  $16 \text{ km s}^{-1}$ . The average amplitudes are low as expected for a depression in the gas, ranging from 2.2 (component 1) to 5.2 mJy/B (component 2). The components are separated by 18, 14, and  $13 \text{ km s}^{-1}$  on average. The high dispersions associated with this region are reflected in these spectra; the gas seems to be somewhat churned up.

With these complex spectra, we do not believe that we detect expansion in the hole. The hole itself is not clearly identifiable in the channel maps, nor is there any feature in the position-velocity diagrams at the location and velocity ( $\sim 350\text{-}360 \text{ km s}^{-1}$ ) of the hole that would indicate expansion or even blowout (e.g. Walter & Brinks 1999).

## 4. Discussion

### 4.1. Current Star Formation and its Relationship to the Gas

In Figure 21 we show contours of H I from the C-configuration map superposed on our H $\alpha$  image. We see that many of the H II regions, including the brightest ones, are located on a ridge of H I and in an H I complex to the south that together appear to form a partial ring around the center of the galaxy. These H II regions are found within an observed H I column density exceeding  $1 \times 10^{21} \text{ cm}^{-2}$ . In addition, the H II regions are primarily associated with local peaks in the H I. This association of star-forming regions with local H I peaks with observed column densities higher than  $10^{21} \text{ cm}^{-2}$  is often seen in Im galaxies. Hunter et al. (2001) argue that the formation of gas clouds in Im galaxies may be aided by the minimal levels of shear in these systems.

In Figure 22 we compare the integrated H I and H $\alpha$  brightnesses of individual pixels in the galaxy. The integrated C-configuration H I map was geometrically matched to the H $\alpha$  image. Then both were averaged  $20 \times 20$  in order to approximately match the H I beam of the

C-configuration map. The beam size is  $14'' \times 11''$ ; and the pixel scale of the averaged maps was  $9.8''$ . The x-axis of this figure goes from an observed H I column density of  $4.3 \times 10^{20} \text{ cm}^{-2}$  to  $1.4 \times 10^{21} \text{ cm}^{-2}$ . The y-axis goes from an H $\alpha$  luminosity of  $9.8 \times 10^{33} \text{ ergs s}^{-1}$  to  $2.5 \times 10^{35} \text{ ergs s}^{-1}$ , corrected for reddening (1 count in the H $\alpha$  image is  $1.95 \times 10^{33} \text{ ergs s}^{-1}$ ; we have not converted this to a surface brightness by dividing by the area of the pixel). H $\alpha$  is corrected for reddening assuming  $E(B-V)_t = E(B-V)_f + 0.1 = 0.155$ . With a Cardelli et al. (1989) reddening curve,  $A_{H\alpha} = 0.48$ . There is a slight trend that the highest H $\alpha$  luminosities are found at the highest observed H I column densities. This is similar to what was found for NGC 2366 (Hunter et al. 2001).

However, in DDO 43 there are also H II regions found at lower column densities and not associated with any apparent peak in H I. There are two small H II regions in the northeast part of the galaxy that lie at H I column densities of about  $7 \times 10^{20} \text{ cm}^{-2}$ . In addition there are several H II regions lying in the central H I holes, also at column densities of  $7 \times 10^{20} \text{ cm}^{-2}$ . One would expect that cloud formation in these regions would be harder because of the lower column densities, especially so for the outer H II regions where the critical gas density for gravitational instabilities is dropping (Safronov 1960, Toomre 1964).

## 4.2. The Holes in the Gas

We have identified four holes in the H I in DDO 43. The largest has a diameter of 850 pc and the smallest is only 110 pc in size. Holes have been found in the H I maps of other disk galaxies as well. Im galaxies with cataloged gas holes include IC10 with 8 holes (Wilcots & Miller 1998), DDO 47 with 19 holes (Walter & Brinks 2001), DDO 50 with 51 holes (Puche et al. 1992), DDO 81 with 48 holes (Walter & Brinks 1999), NGC 6822 with one hole (de Blok & Walter 2000), and the LMC with many holes (Kim et al. 1999). Some of the holes in these galaxies reach 2.0 kpc in diameter, but most are several hundred parsecs in size. Thus, the H I holes in DDO 43 are typical in size. However, we have not detected the signature of expansion in any of DDO 43’s holes. Therefore, they must be relatively old.

DDO 43’s largest hole (“Hole 1”) resembles that surrounding the OB association NGC 206 (=OB78) in M31 (Brinks 1981). The H I hole around NGC 206 has clearly been produced by the mechanical energy input from the concentration of massive stars in the enclosed OB association. Not only do massive stars explode as supernovae, but they dump a comparable amount of energy into their surroundings over their lifetimes in the form of strong winds. Brinks estimates that  $2 \times 10^6 M_{\odot}$  of H I is “missing” from the NGC 206 hole. If we assume that the column density prior to the formation of DDO 43’s hole was the same as the average we see in the knots ( $1.3 \times 10^{21} \text{ cm}^{-2}$ ), and covered the area out to the current  $0.8 \times 10^{21} \text{ cm}^{-2}$

contour, then the amount of H I that is now “missing” is also about  $2 \times 10^6 M_{\odot}$ . The similarity between Hole 1 and the hole around NGC 206 implies that a large OB association like NGC 206 is capable of producing Hole 1. While NGC 206 is a substantial OB association and would have dominated DDO 43’s optical appearance when it was young, it is not an unusual or extreme event and would not have contributed more than 0.08% to the mass of stars in the galaxy. The smaller holes in DDO 43 would have been produced by more modest OB associations.

We measured the UBV colors of the stellar population within Hole 1 using a  $5.7''$  radius aperture centered on the H I position. The colors are  $(B-V)_0 = 0.35 \pm 0.04$  and  $(U-B)_0 = -0.20 \pm 0.05$ .  $(B-V)_0$  is nearly the same as that of the galaxy as a whole, but  $(U-B)_0$  is 0.1 mag redder. These colors do not yield a consistent age for the stellar population, assuming a single star-forming event, perhaps because of contamination by a background galaxy population. However, the slightly redder color of the hole compared to the rest of the galaxy is consistent with an average age of the stellar population in the hole that is a little older than the surroundings. The star-forming event that formed Hole 1 must be old enough that we do not, at least at our modest spatial resolution, see an obvious remnant of the OB association. On the other hand, the age must be young enough that the H I hole is still distinct and has not yet filled back in.

Wada, Spaans, & Kim (2000) have suggested a mechanism for producing holes in the interstellar medium of Im galaxies that does not depend on the energy input from massive stars. They argue that holes can be caused by nonlinear evolution of the multi-phase interstellar medium. This search for a non-stellar production mechanism for holes was motivated by the lack of evidence for aging OB associations in some of the holes in DDO 50. The hole in NGC 6822 also presents a problem because it is located in the outer parts of the optical galaxy. While we cannot rule out this sort of mechanism for the production of the holes in DDO 43, the modest star-forming events needed to produce these holes are likely events in the evolution of an Im galaxy like DDO 43. Therefore, we do not need to invoke other mechanisms.

The gas holes in DDO 43 are located near the center of the galaxy. A ridge of H I surrounds the holes to the north on three sides and a large H I complex sits to the south. The ridge and complex together give one the impression of a ring that is  $2.7 \text{ kpc} \times 2.0 \text{ kpc}$ . Because the center of the ring is composed of several distinct holes rather than a single one, it seems likely that the ring is a consequence of multiple star-forming events that have taken place near the center of the galaxy. The gas shells that resulted have run into each other to give the appearance we have today. Furthermore, this would be a natural means for producing the enhanced H I density that we see in the ring. The ring is where most

of the star formation is taking place today. In this scenario, the star formation in the ring would represent a second generation and would be an example of star-induced star formation (Gerola, Seiden, & Schulman 1980).

DDO 43 is not alone in containing a large gas ring. DDO 88 contains a beautifully complete ring 3.0 kpc in diameter (Simpson et al. 2005). In addition NGC 2366 appears to have a partially broken ring that is 5.5 kpc in diameter (Hunter et al. 2001), and M81dwA and SagDIG have partial rings of 2 kpc and 1 kpc diameter (Sargent, Sancisi, & Lo 1983; Young & Lo 1997).

## 5. Summary

DDO 43 optically resembles other dwarf galaxies that fall at the faint end of the Im distribution. It is relatively isolated, with 270 pc to the nearest Im and 1.6 Mpc to the nearest large galaxy (a spiral). It probably hosts a large stellar bar: it exhibits boxy elliptical isophotes with a small shift in position angle proceeding from the inner to outer regions, and there is an almost  $90^\circ$  misalignment between the optical (bar) axis and the kinematic axis determined from the H I data. Although the bar is large at  $0.8R_{25}$ , galaxy-sized bars are often seen in Ims that have bars. The UVB surface photometry reveals an exponential disk with a normal central surface brightness and an not-unusual scale length of 430 pc. The galaxy’s integrated colors are normal, and like many small systems it exhibits little color gradient across the disk. There are six star clusters visible on the V image. Based on their colors, evolutionary track models indicate that only one is possibly large enough to be considered a “populous” cluster; all the others are relatively small.

In the H I, DDO 43’s extended H I is emphasized by its large  $R_{HI}/R_H$  ratio. There is an extensive, low-level H I envelope containing a high density ridge surrounding the center of the galaxy. This ridge contains higher density knots and lower density depressions in the H I. 44% of the total H I mass is located within this ridge, defined as the region having a column density in excess of  $1 \times 10^{21} \text{ cm}^{-2}$ . We have identified six knots with  $N_{HI} \geq 1.2 \times 10^{21} \text{ cm}^{-2}$ ; the largest knot is roughly  $750 \times 400$  pc across. There are four “holes,” the largest, located just north of the largest H I knot, is 850 pc across. Holes of this size are often detected in Ims and are thought to be the result of star formation activity.

The largest hole in DDO 43 resembles the one formed by star formation that surrounds the OB association NGC 206 in M31. However, there are no young star associations in DDO 43’s holes; the stellar colors are slightly redder than those in the rest of the galaxy and they do not appear to be expanding, so they must be relatively old. The knots in the high density

ridge form a broken ring interspersed with the holes. The structure of knots and holes we see today is most likely the result of the overlapping of expanding H I shells caused by the stellar winds and supernovae explosions from earlier star formation episodes. Most of the current star formation is taking place in the ridge, possibly induced by the sweeping up of gas as the holes were formed.

DDO 43’s current star formation rate is normal, falling in the middle range for Ims. There are several moderate-size H II regions scattered around the galaxy, but there is on average less star formation activity in the inner 0.75 kpc than expected based on a comparison of the azimuthally-averaged H $\alpha$  and V-band surface densities. Most of the H II regions are located in areas of high H I surface density, and many of those are located near local peaks in the H I, as is seen in other Ims. A few of the H II regions are associated with lower H I surface density areas however, including the H I holes.

Kinematically, there is nothing strikingly unusual about DDO 43. It is undergoing the primarily solid-body rotation seen in many dwarfs, with an S-distortion visible in the velocity field, possibly indicating the presence of a warp in the gas disk. The rotation curve levels off and possibly turns over. The maximum rotation velocity is 25 km s<sup>-1</sup>, which is higher than the original estimate. It was the low rotation velocity for its luminosity that caused this galaxy to be classified as a candidate “fossil” tidal dwarf. Dwarf galaxies formed from tidal interactions are predicted to contain less dark matter than primordially formed dwarfs, so should have lower total masses and subsequently, lower rotation speeds. However, the revised velocity estimate puts it back in the normal area of the Tully-Fisher relation for Ims, so there is no reason to think that DDO 43 formed from an interaction.

The dispersion velocities in the H I indicate an average of  $\sim 10$  km s<sup>-1</sup>, which is normal. There is one area of higher dispersion; this is associated with the large hole. The H I spectra through the hole indicate that the gas motions are complex, with most of the spectra exhibiting four peak components. If the hole was produced by star formation activity, it would seem that the gas is still somewhat unsettled.

Overall, DDO 43 is a fairly typical gas-rich, optically faint, small dwarf galaxy. It has an extensive gas disk and a high  $M_{HI}/L_B$  ratio. The H I has been sculpted into a high density ridge forming a partial ring that contains knots and holes. This is most likely the result of multiple episodes of star formation at various times. The mechanical energy deposited in the gas has carved out regions of lower gas density as gas was swept up into expanding shells. High density regions occur where the shells have overlapped. As a result, star formation was triggered in these areas as current star formation activity is located there. The shells are not currently expanding, so the events that formed them must have happened long ago. The current star formation rate is modest; coupled with the large gas reservoir and modest sizes

of the older clusters seen in V, it seems that DDO 43 has evolved slowly, and will continue to do so for the next several Gyr.

We wish to thank Emily Bowsher for examining the color ratio images of DDO 43 as part of the 2003 Research Experiences for Undergraduates program of Northern Arizona University. DAH obtained partial support for this research from the Lowell Research Fund. Additional support to DAH, support for TEN, and support for travel to Flagstaff for CES came from grant AST-0204922 from the National Science Foundation.

This research has made use of the NASA/IPAC Extragalactic Database (NED) which is operated by the Jet Propulsion Laboratory, California Institute of Technology, under contract with the National Aeronautics and Space Administration.

## REFERENCES

- Athanassoula, E., Morin, S., Wozniak, H., Puy, D., Pierce, M. J., Lombard, J., & Bosma, A. 1990, *MNRAS*, 245, 130
- Barnes, J. E., & Hernquist, L. 1992, *Nature*, 360, 715
- Billett, O. H., Hunter, D. A., & Elmegreen, B. G. 2002, *AJ*, 123, 1454
- Brinks, E. 1981, *A&A*, 95, L1
- Burstein, D., & Heiles, C. 1984, *ApJS*, 54, 33
- Cardelli, J. A., Clayton, G. C., & Mathis, J. S. 1989, *ApJ*, 345, 245
- Carignan, C., Beaulieu, S., & Freeman, K. C. 1990, *AJ*, 99, 178
- Combes, F., & Elmegreen, B. G. 1993, *A&A*, 271, 391
- Condon, J. J., Cotton, W. D., Greisen, E. W., Yin, Q. F., Perley, R. A., Taylor, G. B., & Broderick, J. J. 1998, *AJ*, 115, 1693
- de Blok, W. J. G., & Walter, F. 2000, *ApJ*, 537, L95
- de Jong, R. S. 1996, *A&A*, 313, 45
- de Vaucouleurs, G., de Vaucouleurs, A., Corwin, H., Buta, R., Paturel, G., & Fouqué, P. 1991, *Third Reference Catalogue of Bright Galaxies* (New York, Springer-Verlag), =RC3
- Duc, P.-A., & Mirabel, L. F. 1999, in *Galaxy Interactions at High and Low Redshift*, eds. J. E. Barnes & D. B. Sanders (Kluwer), p 61
- Elmegreen, B. G., & Elmegreen, D. M. 1985, *ApJ*, 288, 438
- Elmegreen, B. G., Elmegreen, D. M., Chromey, F. R., Hasselbacher, D. A., & Bissell, B. A. 1996, *AJ*, 111, 2233
- Gerola, H., Seiden, P. E., & Schulman, L. S. 1980, *ApJ*, 242, 517
- Huchtmeier, W. K., & Richter, O.-G. 1986, *A&AS*, 63, 323
- Huchtmeier, W. K. & Richter, O.-G. 1989, *A General Catalog of H I Observations of Galaxies. The Reference Catalog, XIX* (New York: Springer-Verlag)
- Hunsberger, S. D., Charlton, J. C., & Zaritsky, D. 1996, *ApJ*, 462, 50
- Hunter, D. A. 1997, *PASP*, 109, 937
- Hunter, D. A., & Elmegreen, B. G. 2004, *AJ*, 128, 2170
- Hunter, D. A., Elmegreen, B. G., & Baker, A. L. 1998, *ApJ*, 493, 595
- Hunter, D. A., Elmegreen, B. G., & van Woerden, H. 2001, *ApJ*, 556, 773

- Hunter, D. A., & Hoffman, L. 1999, *AJ*, 117, 2789
- Hunter, D. A., Hunsberger, S. D., & Roye, E. W. 2000, *ApJ*, 542, 137
- Hunter, D. A., Rubin, V. C., Swaters, R. A., Sparke, L. S., & Levine, S. E. 2002, *ApJ*, 580, 194
- Hunter, D. A., van Woerden, H., & Gallagher, J. S. 1999, *AJ*, 118, 2184
- Kennicutt, R. C. 1984, *ApJ*, 287, 116
- Kennicutt, R. C., Balick, B., & Heckman, T. 1980, *PASP*, 92, 134
- Kim, S., Dopita, M.A., Staveley-Smith, L., & Bessell, M.S. 1999, *AJ*, 118, 2797
- Landolt, A. U. 1992, *AJ*, 104, 340
- Leitherer, C., Schaerer, D., Goldader, J. D., González Delgado, R. M., Robert, C., Kune, D. F., de Mello, D. F., Devost, D., & Heckman, T. M. 1999, *ApJS*, 123, 3
- Malphrus, B., Simpson, C. E., Gottesman, S. T., & Hawarden, T. G. 1997, *AJ*, 114, 1427
- Martin, C. L. 1998, *ApJ*, 506, 222
- Martin, P. 1995, *AJ*, 109, 2428
- Meurer, G. R., Freeman, K. C., & Dopita, M. A. 1992, *AJ*, 103, 60
- Meurer, G. R., Staveley-Smith, L. & Killeen, N. E. B. 1998, *MNRAS*, 300, 705
- Mirabel, I. F., Dottori, H., & Lutz, D. 1992, *A&A*, 256, L19
- Ott, J., Walter, F., Brinks, E., Van Dyk, S. D., Dirsch, B., & Klein, U. 2001, *AJ*, 122, 3070
- Puche, D., Westpfahl, D., Brinks, E., Roy, J.-R. 1992, *AJ*, 103, 1841
- Rhode, K. L., Salzer, J. J., Westpfahl, D. J., & Radice, L. A. 1999, *AJ*, 118, 323
- Rogstad, D. H., Lockhart, I. A., & Wright, M. C. H. 1974, *ApJ*, 193, 309
- Roye, E. W., & Hunter, D. A. 2000, *AJ*, 119, 1145
- Safronov, V. S. 1960, *Ann.d'Ap.*, 23, 979
- Salpeter, E. E. 1955, *ApJ*, 121, 161
- Sargent, W. L. W., Sancisi, R., & Lo, K. Y. 1983, *ApJ*, 265, 711
- Scalo J., & Chappell, D. 1999, *MNRAS*, 310, 1
- Simpson, C. E., & Gottesman, S. T. 2000, *AJ*, 120, 2975
- Simpson, C. E., Hunter, D. A., & Knezek, P. 2005, *AJ*, 129, 160
- Skillman, E. D., Terlevich, R., Teuben, P. J., & van Woerden, H. 1988, *A&A*, 198, 33
- Stewart, S. G., et al. 2000, *ApJ*, 529, 201



- Stil, J. M., & Israel, F. P. 2002, *A&A*, 389, 42
- Swaters, R. 1999, Ph.D. Thesis, Rijksuniversiteit Groningen
- Toomre, A. 1964, *ApJ*, 139, 1217
- Wada, K., Spaans, M., & Kim, S. 2000, *ApJ*, 540, 797
- Walter, F., & Brinks, E. 1999, *AJ*, 118, 273
- Walter, F., & Brinks, E. 2001, *AJ*, 121, 3026
- Wilcots, E. M., & Hunter, D. A. 2002, *AJ*, 123, 1476
- Wilcots, E. M., & Miller, B. W. 1998, *AJ*, 116, 2363
- Young, L. M., & Lo, K. Y. 1996, *ApJ*, 462, 203
- Young, L. M., & Lo, K. Y. 1997, *ApJ*, 490, 710

Table 1. VLA Observations

	D configuration	C configuration	C+D <sub>UN</sub> <sup>a</sup>	C+D <sub>NA</sub> <sup>a</sup>
Observation Date	1996 Sept. 20	2000 April 9	...	...
Time on Source (min)	274	268	...	...
Bandwidth (MHz)	1.56	1.56	1.56	1.56
No. of Channels	128	128	128	128
Velocity Resolution (km s <sup>-1</sup> )	2.6	2.6	2.6	2.6
Beam Size <sup>b</sup> (")	54.8 × 52.7	14.0 × 11.0	20.3 × 14.4	24.5 × 17.1
Single channel r.m.s. (mJy B <sup>-1</sup> )	0.81	1.05	1.07	1.05
Brightness Temperature (K)	0.24	3.15	...	...

<sup>a</sup>Combined data set from both configurations

<sup>b</sup>Natural weighting for D and C+D<sub>NA</sub>; uniform weighting with robust factor of +1 for C and C+D<sub>UN</sub>

Table 2. Summary of Integrated Properties.

Parameter	Value
D (Mpc) .....	5.5
$M_{HI}$ ( $M_{\odot}$ ) .....	$9.2 \times 10^7$
$E(B-V)_f^a$ .....	0.055
$R_{25}$ (arcsec, kpc) .....	37, 0.99
$R_H$ (arcsec, kpc) .....	53, 1.4
$R_{HI}^b$ (arcsec, kpc) .....	146, 3.9
$\mu_0$ (V-band, mag arcsec $^{-2}$ ) .....	$22.4 \pm 0.2$
$R_D$ (pc) .....	$430 \pm 50$
$M_{V_0}$ (R=57'') .....	$-14.31 \pm 0.02$
(U-B) $_0$ (R=57'') .....	$-0.31 \pm 0.04$
(B-V) $_0$ (R=57'') .....	$0.31 \pm 0.02$
$\log L_{H\alpha,0}$ (ergs s $^{-1}$ ) .....	$38.80 \pm 0.006$
SFR $^c$ ( $M_{\odot}/\text{yr}^{-1}$ ) .....	0.0037
$\log \text{SFR}/\text{area}^c$ ( $M_{\odot} \text{ yr}^{-1} \text{ kpc}^{-2}$ ) .....	-2.91
$M_{HI}/L_B$ ( $M_{\odot}/L_{\odot}$ ) .....	1.64

<sup>a</sup> $E(B-V)_f$  is foreground reddening due to the Milky Way (Burstein & Heiles 1984). For the stars in DDO 43, we assume an additional internal reddening of 0.05 magnitude; for the H II regions we assume an additional internal reddening of 0.1 magnitude, consistent with Balmer decrement observations of emission nebulae in DDO 43 (Hunter & Hoffman 1999).

<sup>b</sup>Measured to  $N_{HI} = 5 \times 10^{19} \text{ cm}^{-2}$ ; corrected for the beam-size.

<sup>c</sup>Star formation rate derived from  $L_{H\alpha}$  using the formula of Hunter & Elmegreen (2004) that integrates from  $0.1 M_{\odot}$  to  $100 M_{\odot}$  with a Salpeter (1955) stellar initial mass function. The area is  $\pi R_{25}^2$ .

Table 3. Star cluster properties.

Cluster	$M_{V_0}$	U–B <sub>0</sub>	B–V <sub>0</sub>	Age (Myr)	$M_V$ (10 Myr) <sup>a</sup>	Nebula? <sup>b</sup>
1	$-8.63 \pm 0.15$	$0.25 \pm 0.21$	$-0.55 \pm 0.21$	7–70	–7.4 to –10.2	N
2	$-6.89 \pm 0.24$	$0.03 \pm 0.32$	$-0.89 \pm 0.24$	3–20	–6.0 to –7.6	N
3	$-8.66 \pm 0.05$	$0.18 \pm 0.07$	$-0.43 \pm 0.07$	7,15	–7.5, –8.8	Y
4	$-9.28 \pm 0.07$	$0.56 \pm 0.12$	$-0.66 \pm 0.13$	8–15:	–8.6 to –9.4	Y
5	$-8.07 \pm 0.13$	$0.05 \pm 0.18$	$-0.68 \pm 0.15$	5–30	–7.1 to –9.1	Y
6	$-8.50 \pm 0.09$	$0.11 \pm 0.11$	$-0.98 \pm 0.08$	5:	–7.5	Y

<sup>a</sup>The  $M_V$  that the cluster will or would have had at an age of 10 Myrs, determined from the ages and the cluster evolutionary track of Leitherer et al. 1999 for a metallicity of  $Z = 0.008$ .

<sup>b</sup>The presence of nebular emission suggests that the younger age in a range is more appropriate.

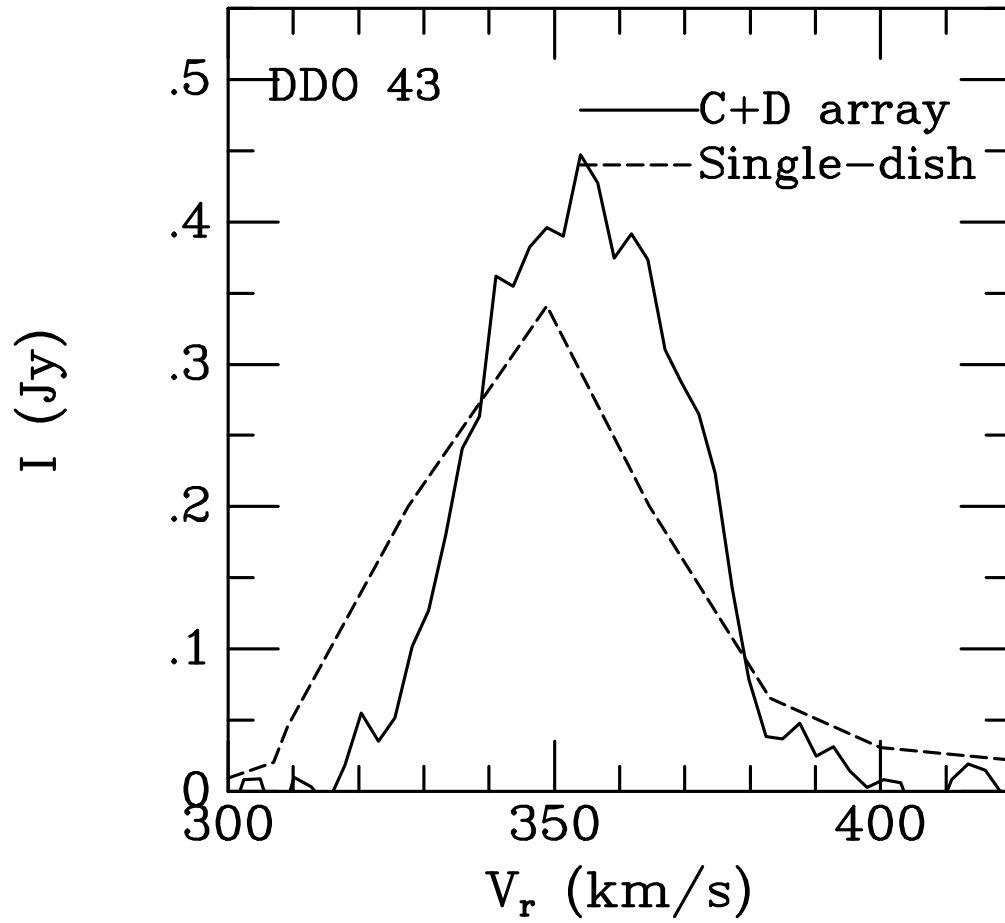


Fig. 1.— Velocity profiles from our C+D-configuration data (natural weighting) and from single-dish data (Huchtmeier & Richter 1986).

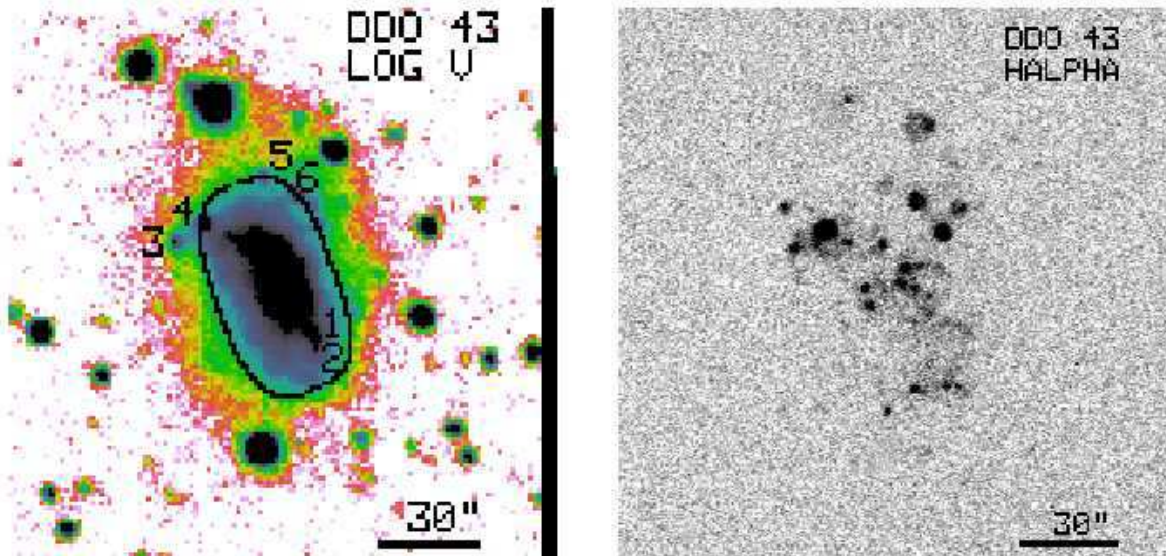


Fig. 2.— Left: False-color display of the logarithm of our V-band image of DDO 43. We display the image this way in order to allow immediate comparison of the inner and outer parts of the galaxy. The smooth elliptical curve superposed in black is the best-fit bar structure with  $c = 3.0$  and a semi-major axis of  $33''$ . Star clusters discussed in the text are numbered. The black columns along the right edge are from a very bright star to the southwest in the larger field of view of the CCD that saturated and bled. Right: Gray-scale display of our  $H\alpha$  image of DDO 43. Stellar continuum has been removed to leave only nebular emission. The field of view and orientation is the same as that of the V-band image. North is up and East is to the left.

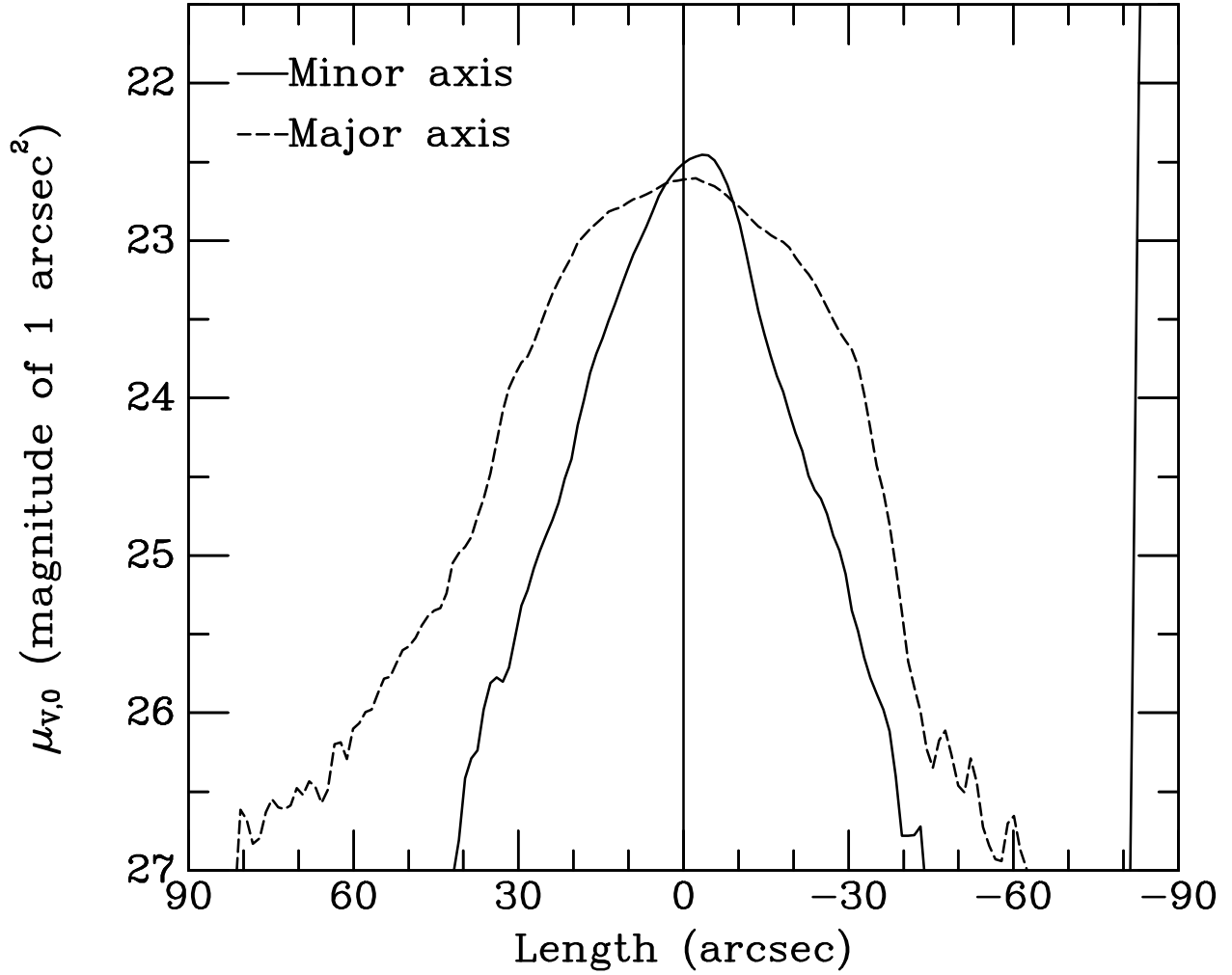


Fig. 3.— Surface brightness cuts along the bar in the V-band image of DDO 43 (Figure 2). Cuts along the major axis (position angle  $20^\circ$ ) and along the minor axis are shown. Both were constructed by averaging over  $20''$ . The surface brightness is corrected for reddening. The left side of the graph refers to the northeast side of the major axis and the southeast side of the minor axis. The spike to the right is due to bleeding columns of a saturated star.

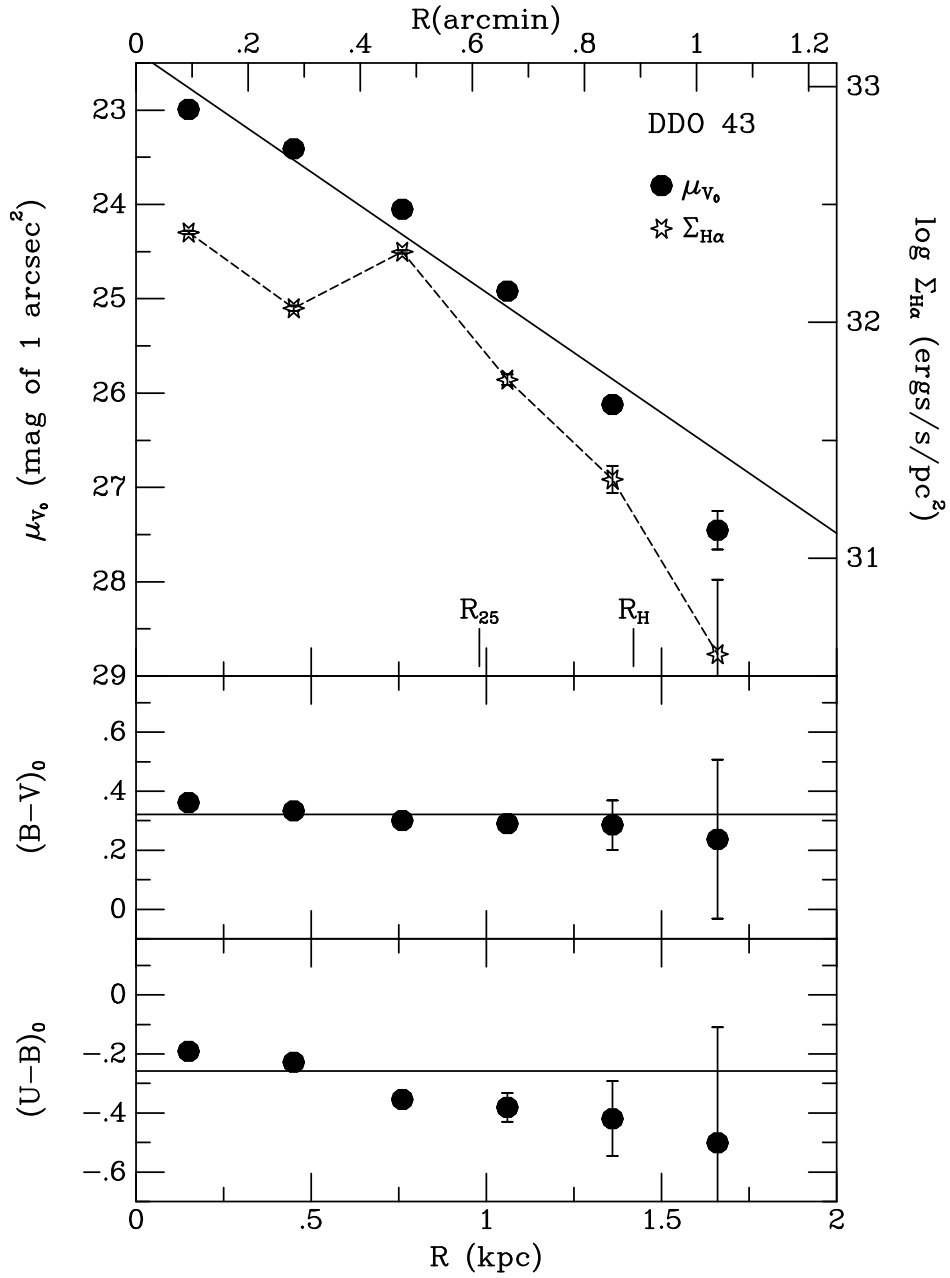


Fig. 4.— UVB and H $\alpha$  azimuthally-averaged surface photometry of DDO 43 integrated in annuli of 11.3'' width. The UVB photometry is corrected for an internal reddening of 0.05 mag and a foreground reddening of 0.055 mag. For H $\alpha$  the internal reddening is taken to be 0.1 mag. The solid line is an exponential fit to the V-band surface brightness profile. The scales for  $\Sigma_{H\alpha}$ , labelled on the right y-axis, and  $\mu_{V_0}$ , labelled on the left y-axis, have been set so that they cover the same logarithmic interval.



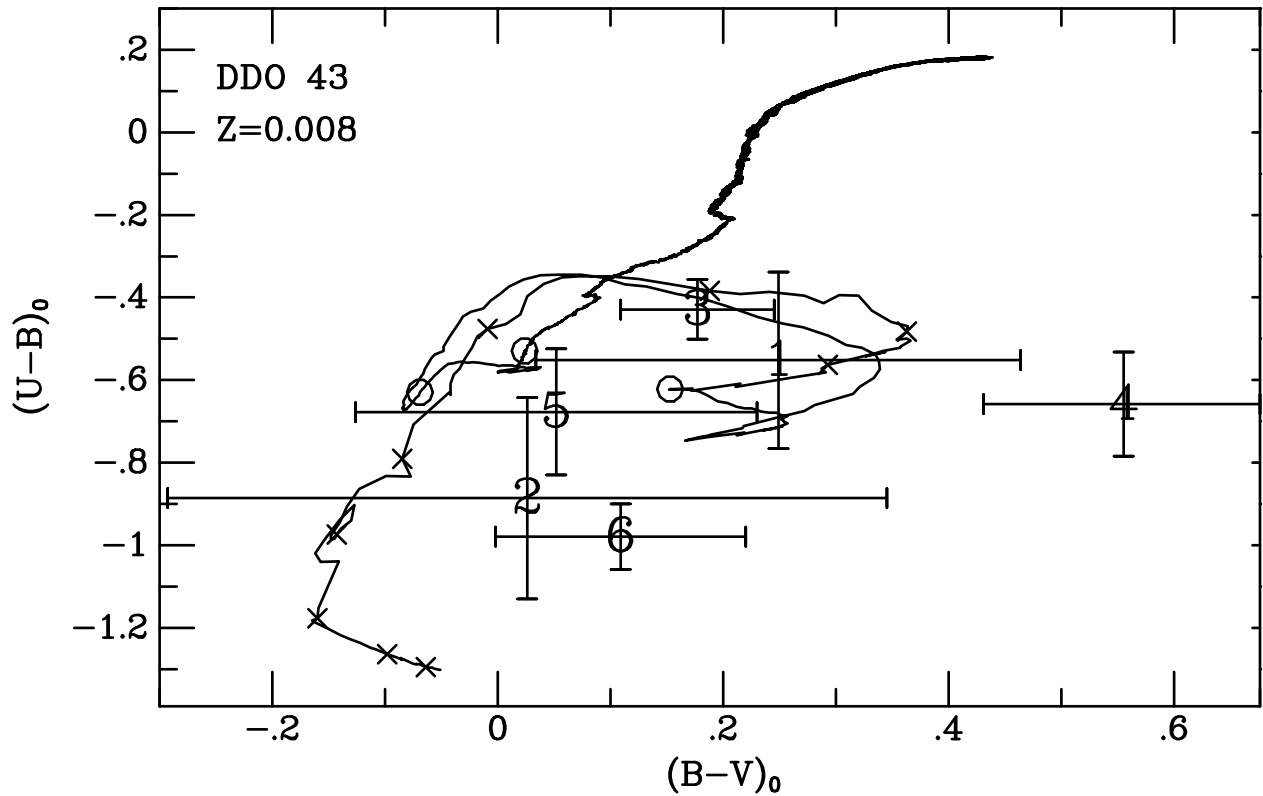


Fig. 5.— UBV color-color diagram with photometry of the star clusters shown. The numbers of the clusters correspond to the labels in Figure 2. The curved solid line is the cluster evolutionary track of Leitherer et al. (1999) for a metallicity of  $Z=0.008$ . The X's on this line mark ages of 1 to 9 Myr in steps of 1 Myr. The open circles on this line mark 10, 20, and 30 Myr time steps.

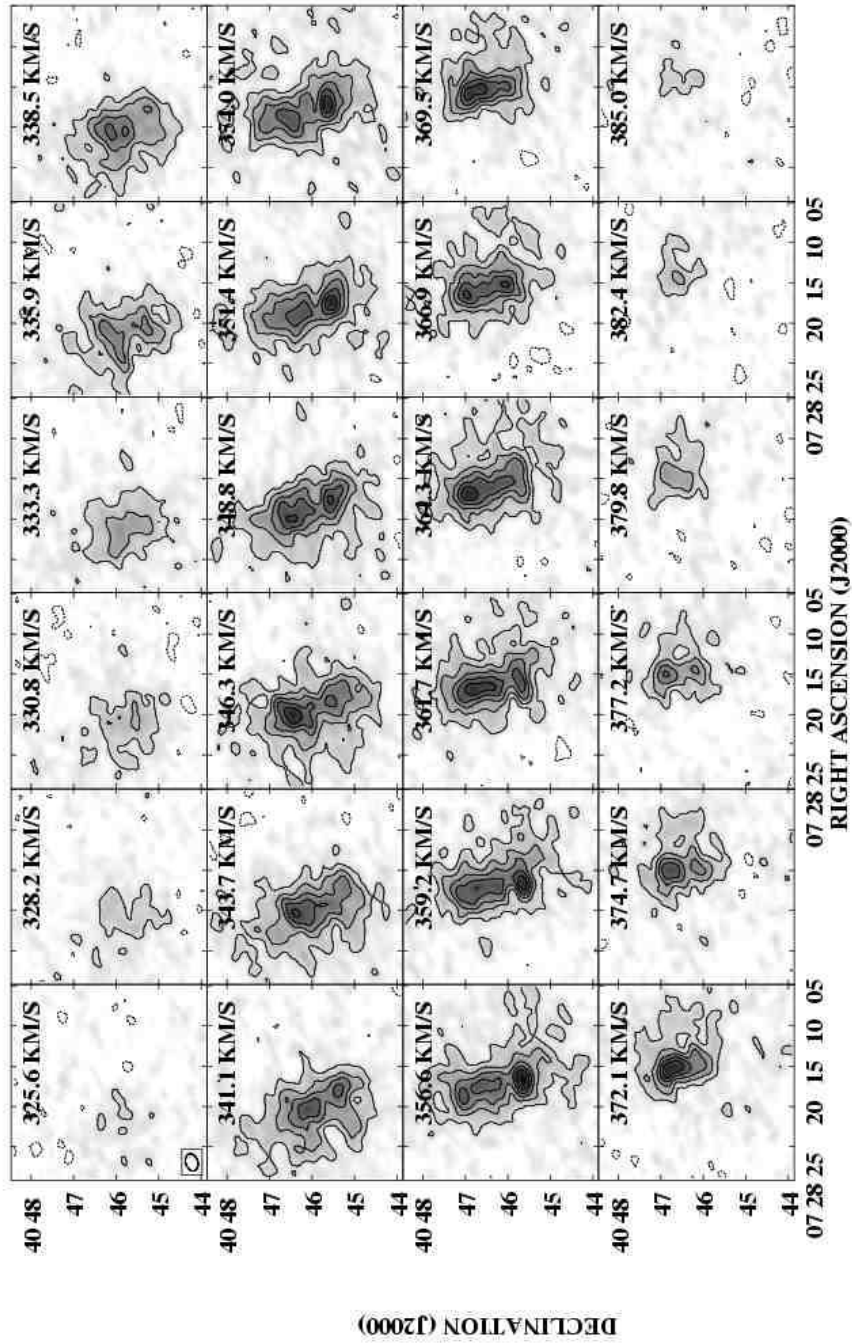


Fig. 6.— Channel maps from the naturally-weighted C+D HI data cube. Each channel is labelled with its heliocentric velocity; the beam FWHM (shown in the lower left corner of the first panel) is  $20.30'' \times 14.4''$ . Contours are drawn at  $-2$  (dashed lines),  $3$ ,  $6$ ,  $9$ ,  $12$ , and  $15\sigma$  where  $1\sigma$  is the measured r.m.s. in a signal-free channel and is  $1.05 \text{ mJy Beam}^{-1}$  for this data cube.

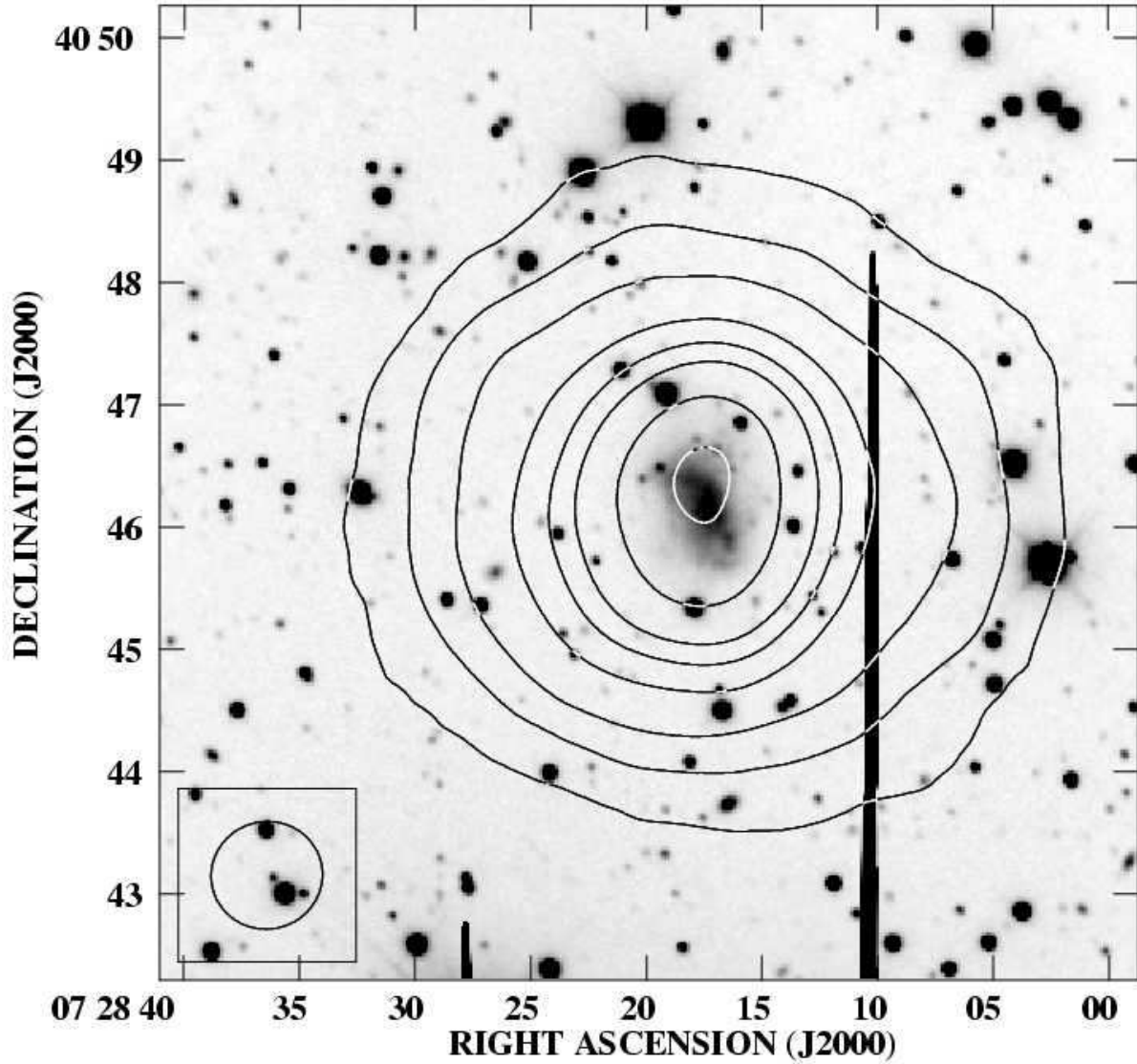


Fig. 7.— Integrated HI flux density contours from the D-configuration naturally-weighted data cube overlaid on the V image. The field of view shown is approximately  $8' \times 8'$ . The beam size (FWHM) is shown in the lower left corner, and measures  $54.83'' \times 52.70''$ . Contours are drawn at  $N_{HI} = 1, 5, 10, 20, 40, 60,$  and  $80 \times 10^{19} \text{ cm}^{-2}$ . ( $1 \times 10^{19} \text{ cm}^{-2} = 26.17 \text{ Jy B}^{-1} \text{ m s}^{-1}$ .)

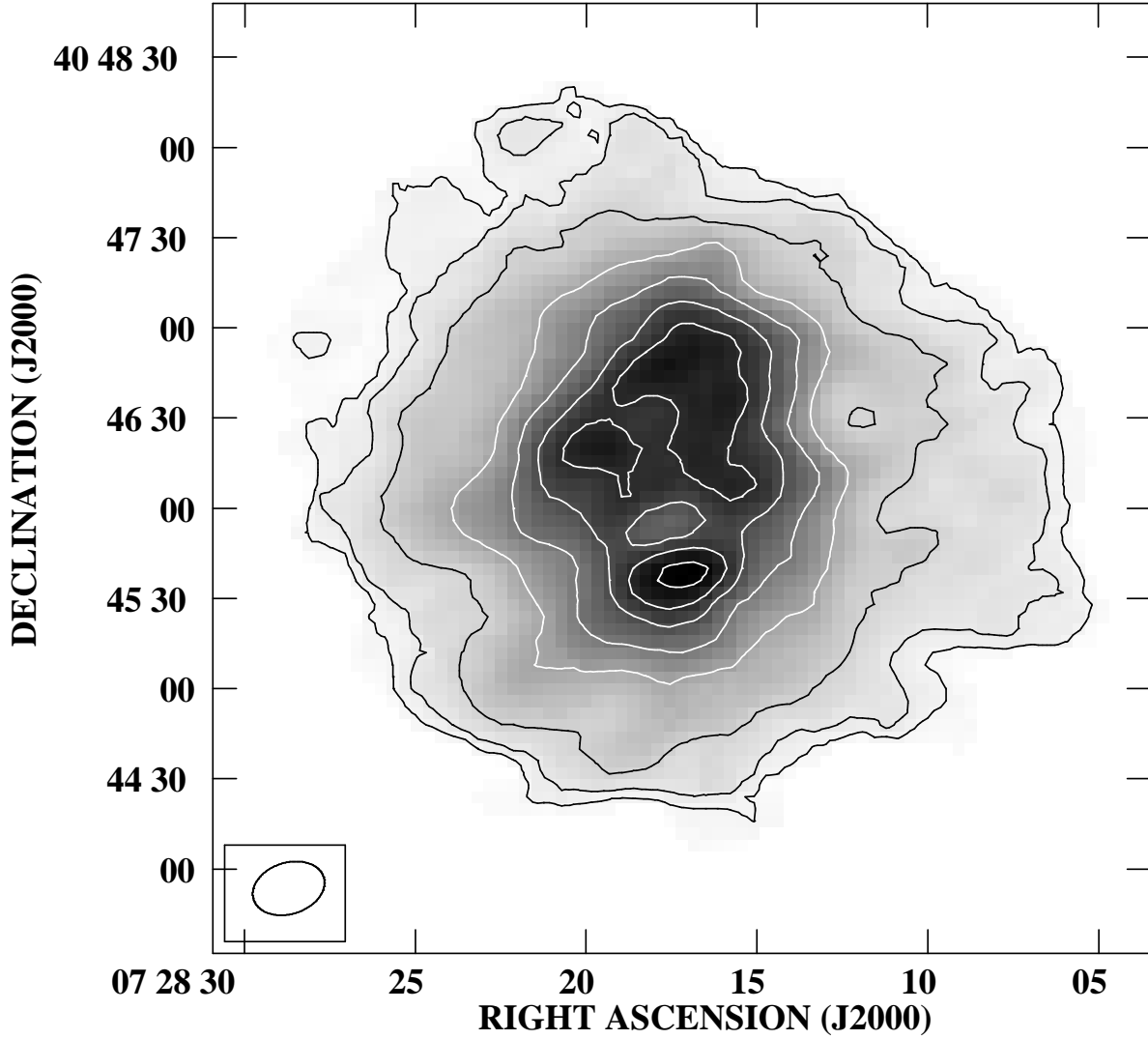


Fig. 8.— Integrated HI flux density from the C+D<sub>NA</sub> cube. The field shown is 5'×5'. The beam size (FWHM shown in the lower left corner) is 24.5''×17.1''. The contours are at  $N_{HI} = 0.5, 1, 2, 4, 6, 8, 9.5,$  and  $11 \times 10^{20} \text{ cm}^{-2}$ , where  $1 \times 10^{19} \text{ cm}^{-2} = 3.79 \text{ mJy Beam}^{-1} \text{ km s}^{-1}$ .

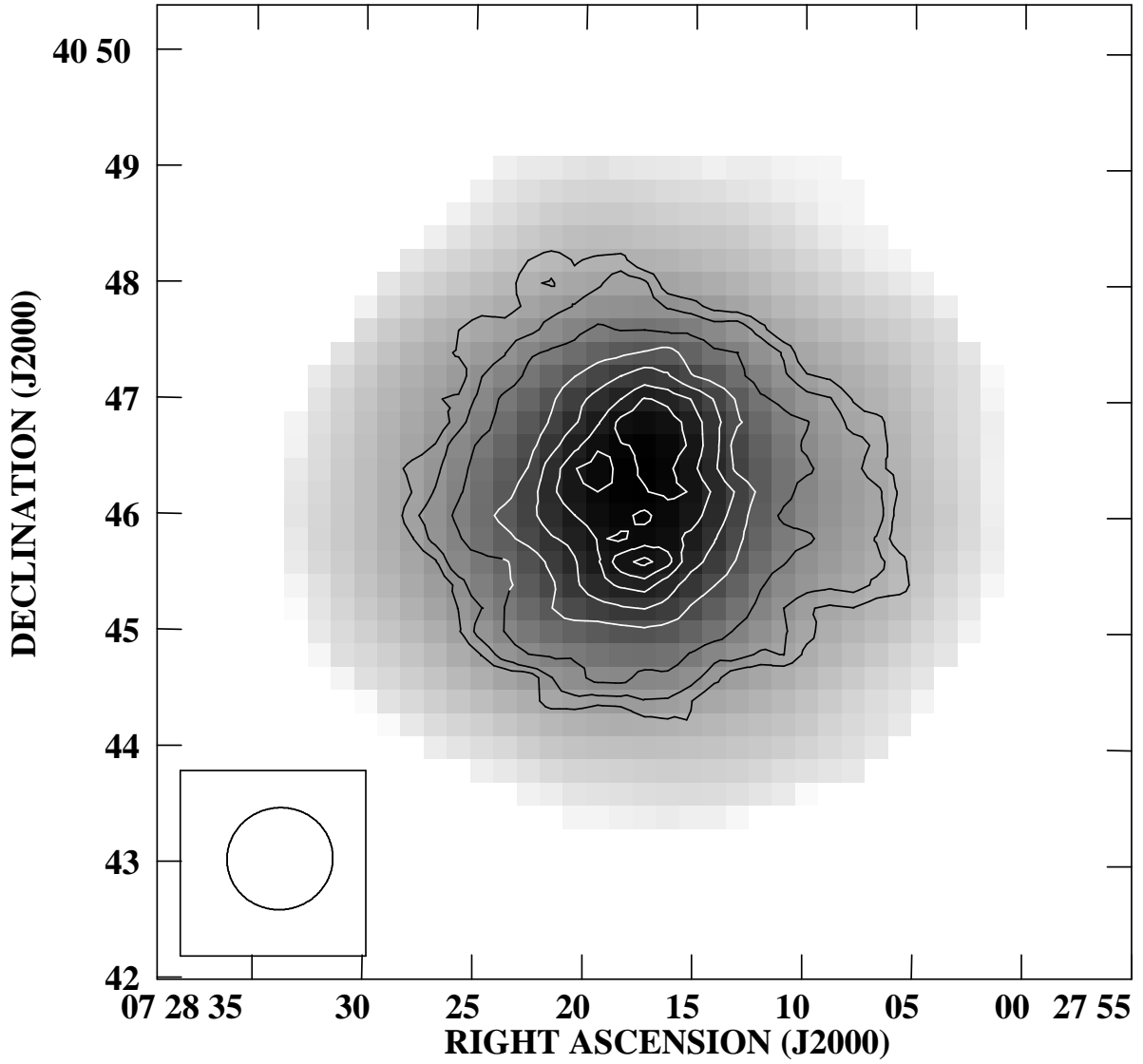


Fig. 9.— D-configuration integrated flux map (greyscale) with contours from the C+D<sub>NA</sub> data map. The field of view shown is approximately 8'×8'. Contours are drawn at the same levels as in Figure 8.

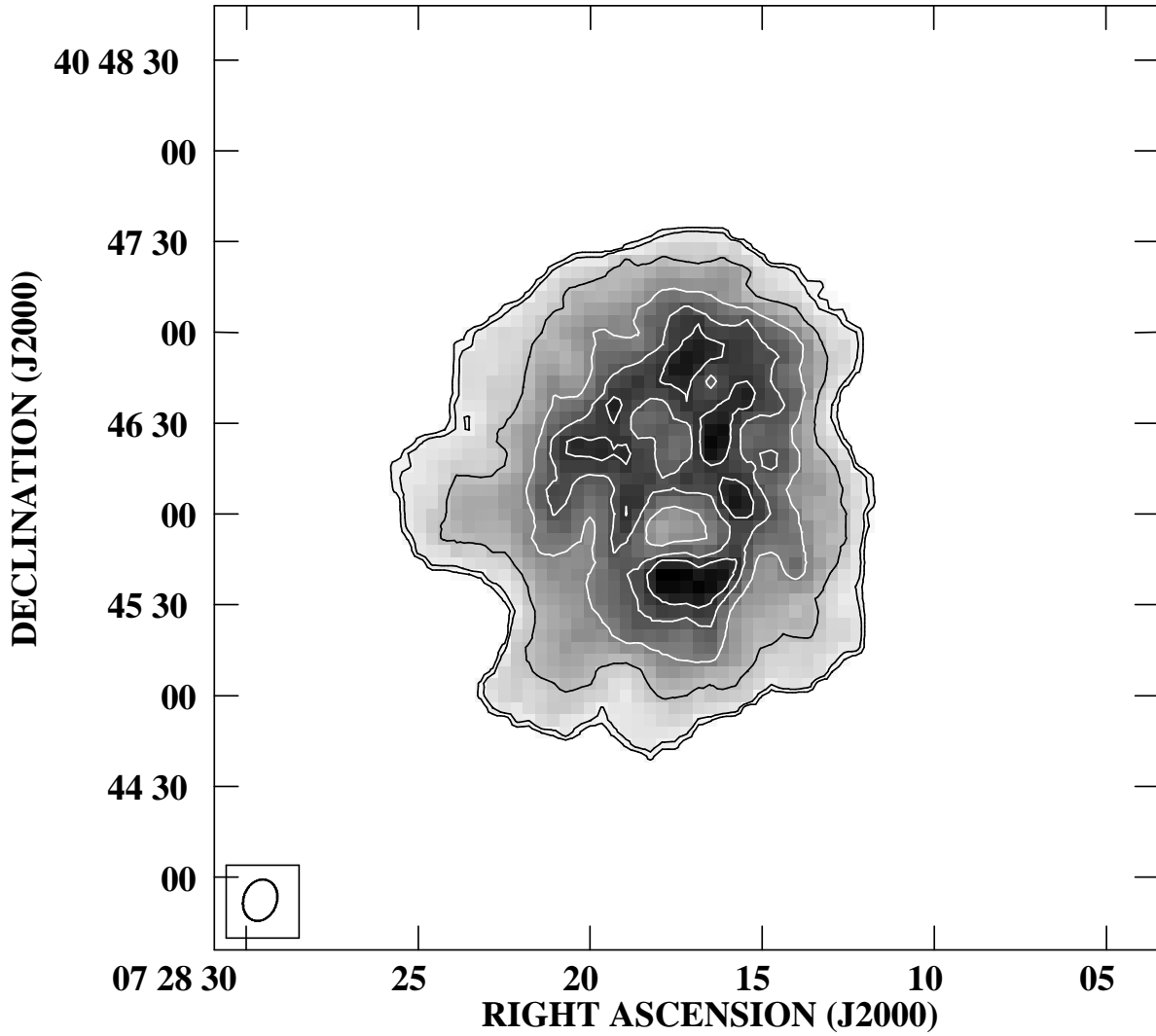


Fig. 10.— Integrated HI flux density from the C configuration data (uniform weighting). The field shown is  $5' \times 5'$ . The beam, indicated in the lower left corner, is  $14.0'' \times 11.0''$ . Contour levels are at 0.5, 1.0, 3.6, 7.2, 10, and  $12 \times 10^{20} \text{ cm}^{-2}$ ;  $1 \times 10^{19} \text{ cm}^{-2} = 1.395 \text{ mJy Beam}^{-1} \text{ km s}^{-1}$ .

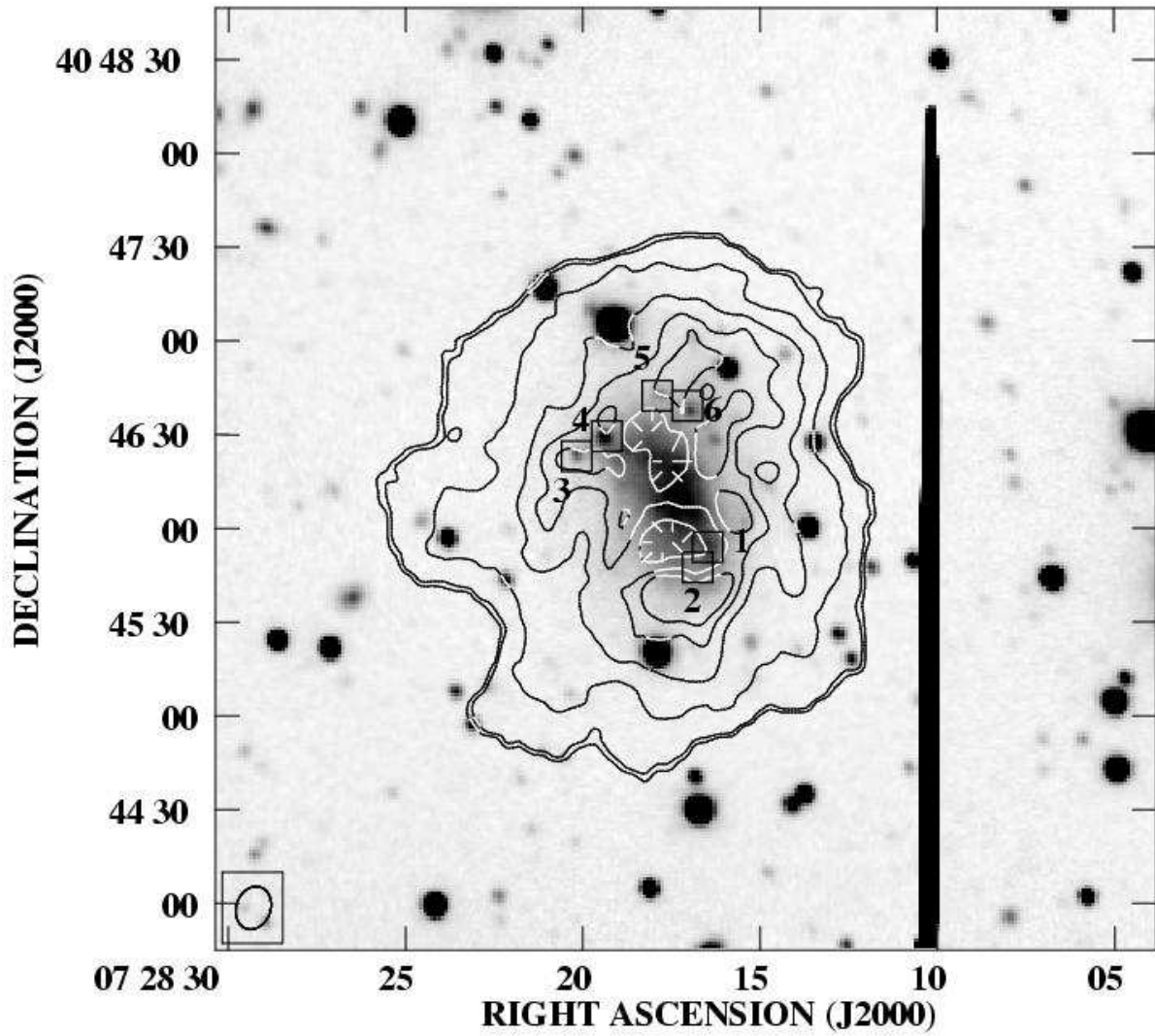


Fig. 11.— C-configuration integrated flux contours on V image. Contours, field, and beam-size are the same as in Figure 10. The two most prominent HI holes are indicated by the contours with the hash marks; the star clusters are marked by the boxes and labelled.

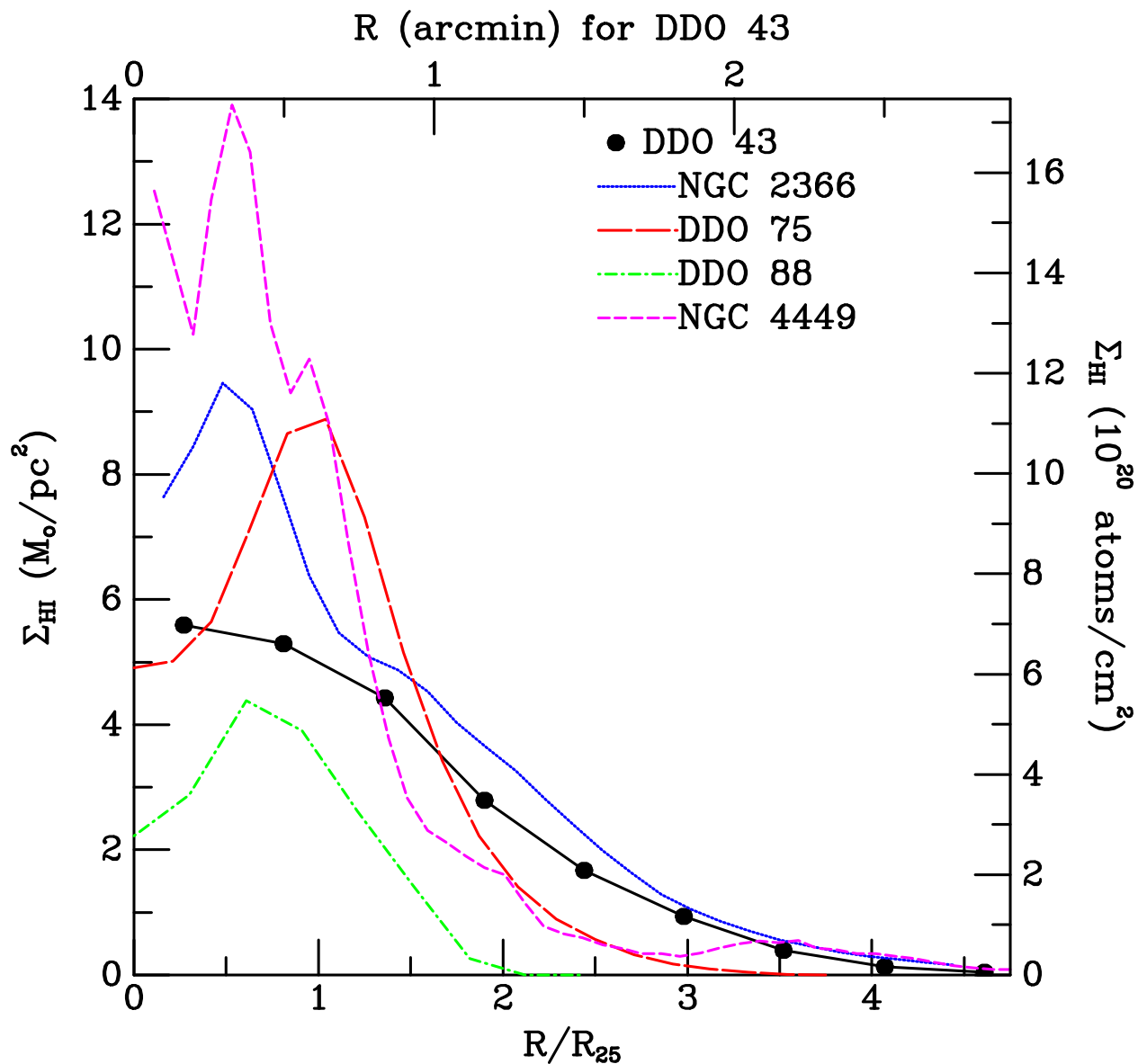


Fig. 12.— Gas surface density in DDO 43 from the C+D<sub>NA</sub> data. The H I surface density has been corrected to include He. For comparison we show gas surface density profiles for DDO 75 (Wilcots & Hunter 2002), DDO 88 (Simpson et al. 2005), NGC 2366 (Hunter et al. 2001), and NGC 4449 (Hunter et al. 1999).



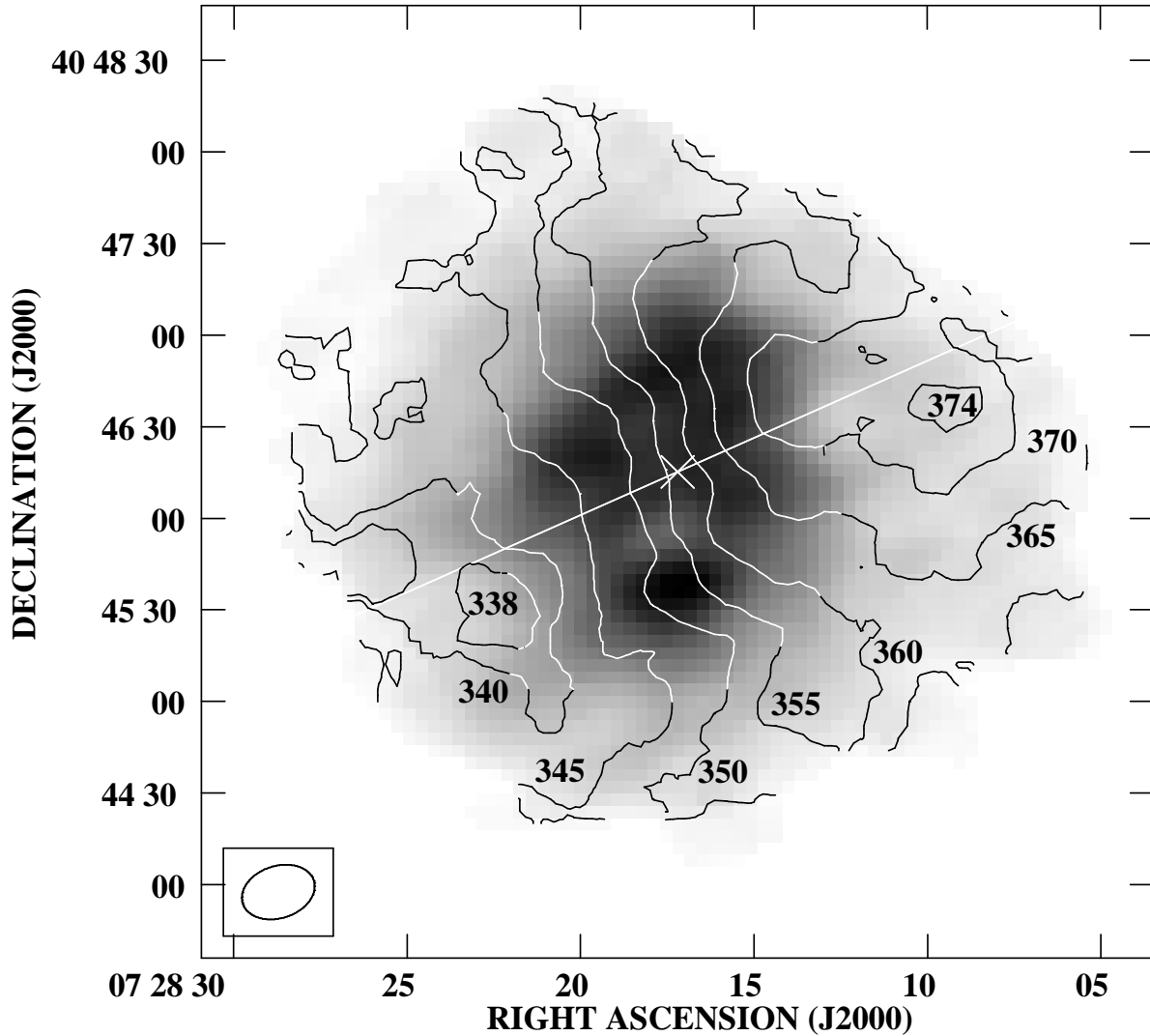


Fig. 13.— Isovelocity contours superposed on an integrated HI flux map of DDO 43. The moment maps were made from the C+D-configuration cube made with natural weighting. Contours are marked with velocity values in  $\text{km s}^{-1}$ . The beam size (FWHM shown in the lower left corner) is  $24.5'' \times 17.1''$  and the velocity resolution is  $2.6 \text{ km s}^{-1}$ . The X marks the kinematic center of the galaxy and the straight line the position angle ( $294^\circ$ ) that were determined in the fit to the velocity field.

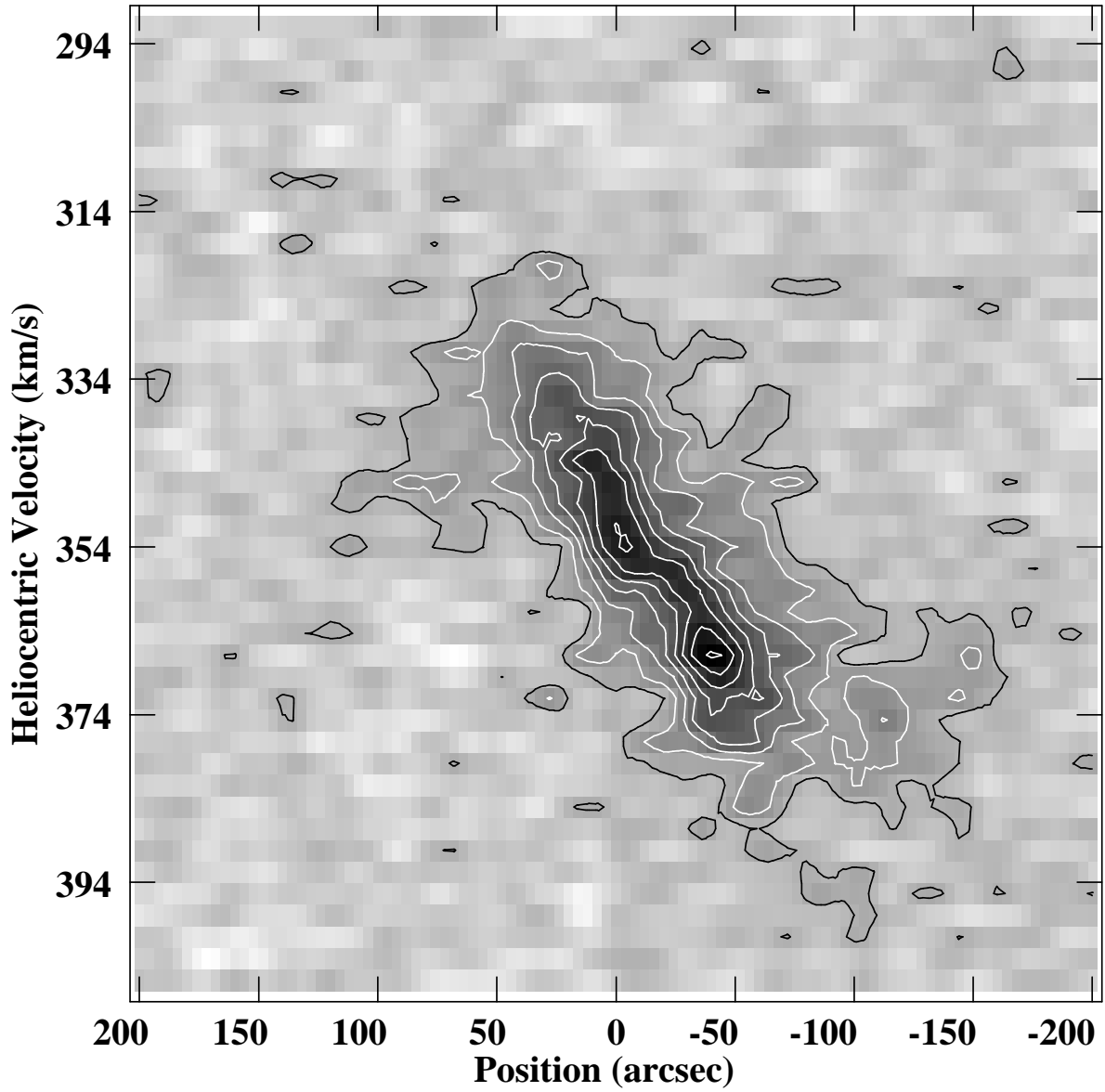


Fig. 14.— Position-velocity cut through the uniformly-weighted C+D-configuration cube of DDO 43. A cut  $20''$  wide was made at a position angle of  $294^\circ$ . Contours are at 2, 4, 6, 8, 10, 12, 14, and 16  $\sigma$ ;  $1\sigma = 3.7$  mJy/B.

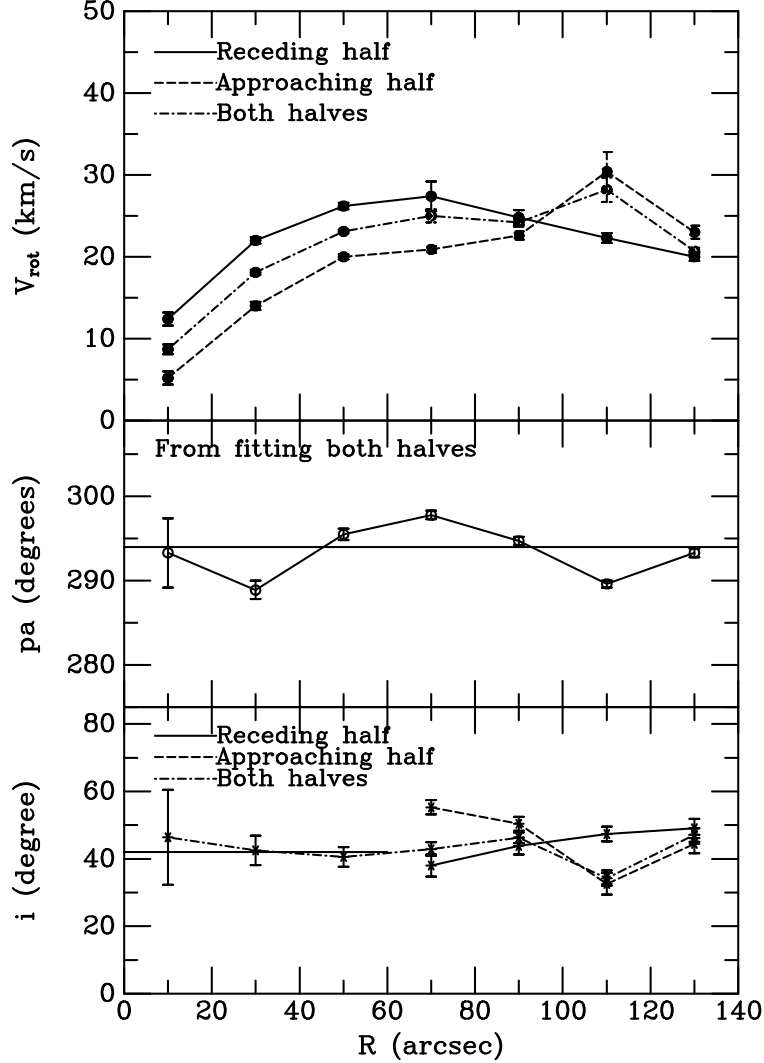


Fig. 15.— Top: Best-fit rotation curve for DDO 43. The rotation curve comes from fitting tilted rings of  $20''$  width. The center position, systemic velocity ( $355 \text{ km s}^{-1}$ ), position angle ( $294^\circ$ ), and inclination ( $42^\circ$ ) interior to a radius of  $60''$  were fixed in the final fit. The inclination beyond  $60''$  was allowed to vary and the values of the inclination are shown in the bottom panel. The kinematics of the approaching side of the galaxy are not well fit by the model. Middle: Position angle determined in tilted rings. These come from fitting both halves of the galaxy with the center position and systemic velocity held fixed. The solid horizontal line marks the average that was then fixed for the rest of the rotation curve determination. Bottom: Variation of inclination in tilted ring models. Interior to a radius of  $60''$  the inclination was fixed at  $42^\circ$ , the average value found from fitting both halves of the galaxy. Beyond  $60''$ , the inclination was allowed to vary in the final determination of the rotation curve.

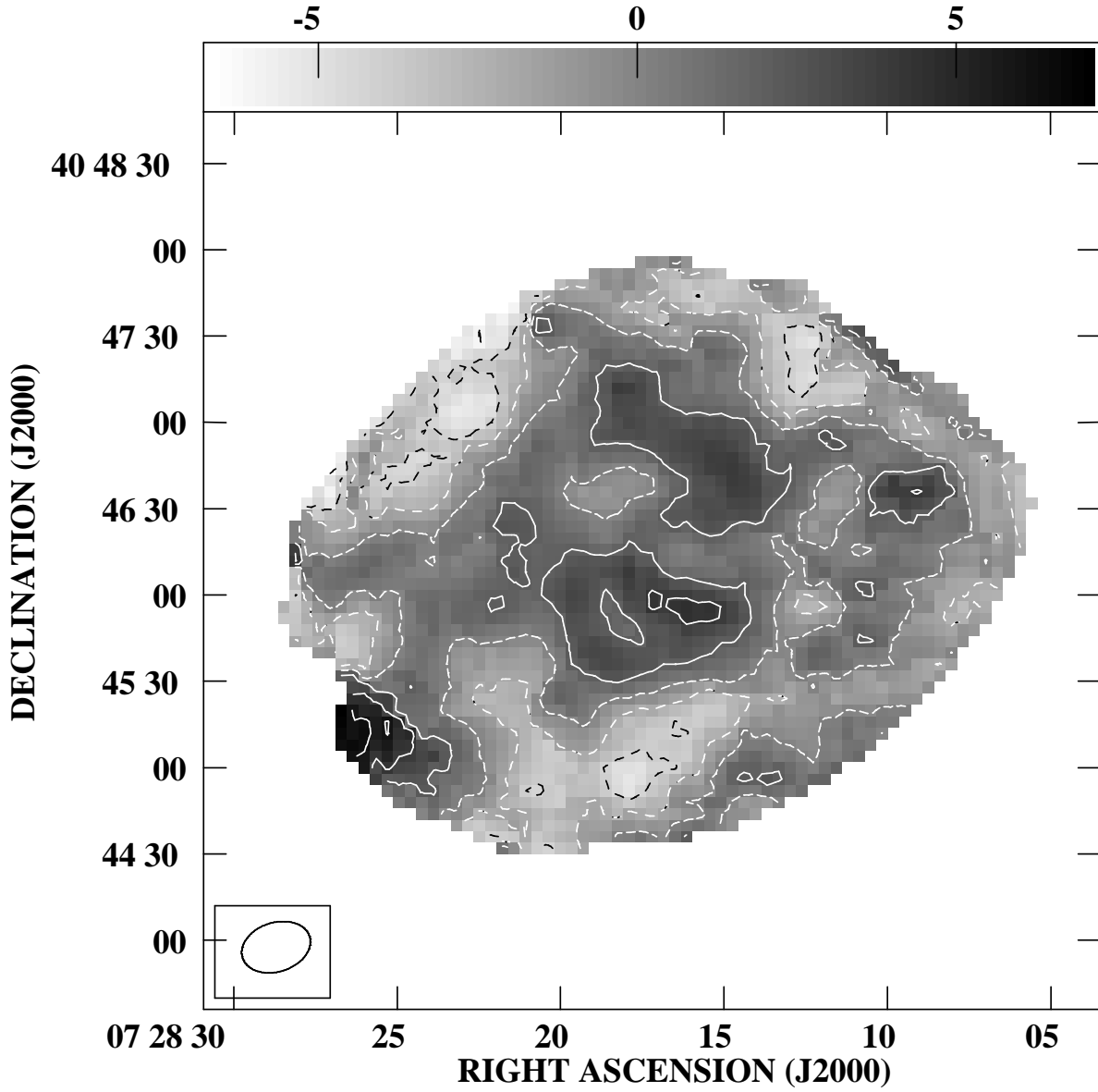


Fig. 16.— Velocity residual map from subtracting the observed velocity from the model. Contours are from  $-6$  to  $+6 \text{ km s}^{-1}$  by  $2 \text{ km s}^{-1}$ .

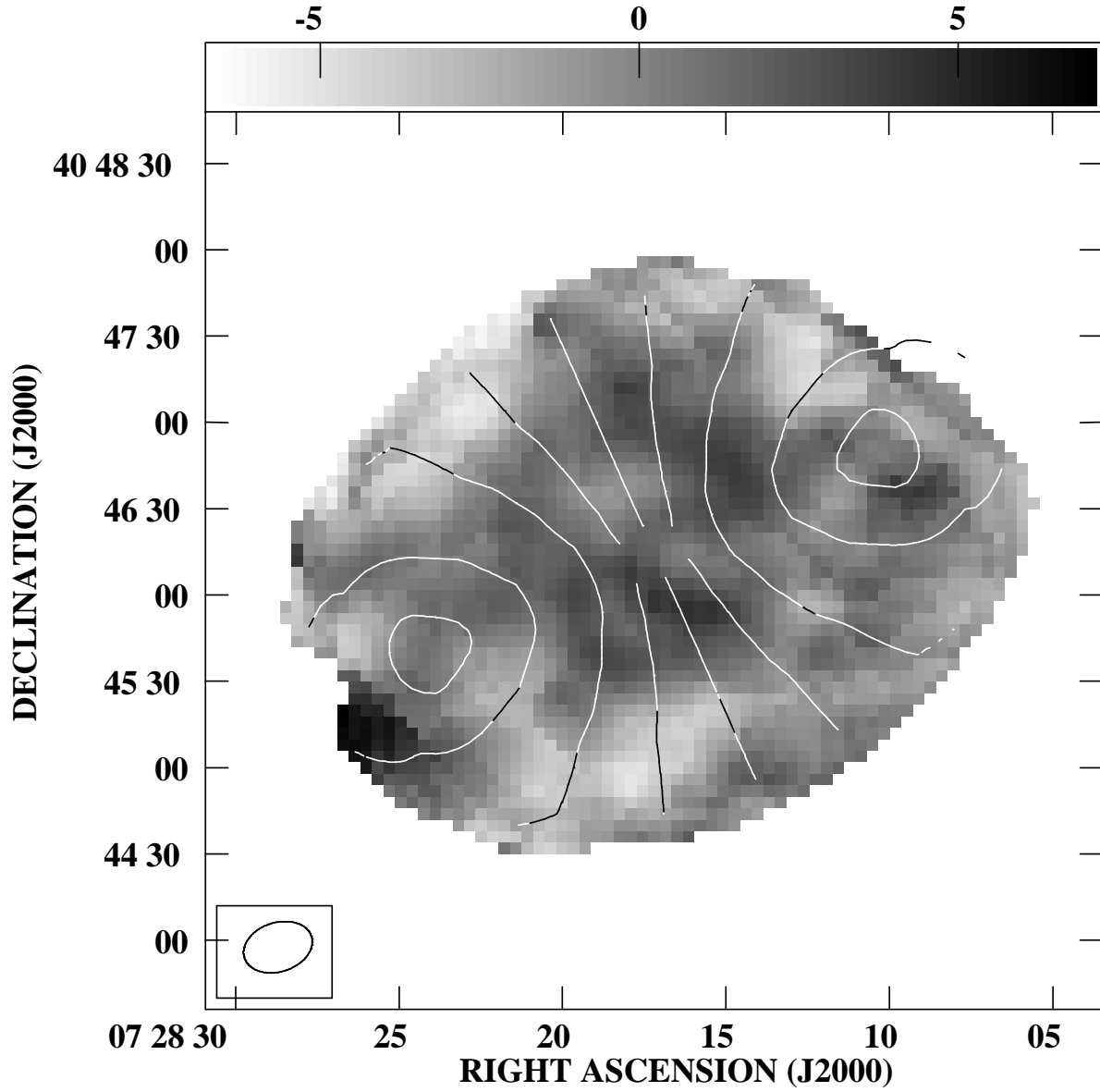


Fig. 17.— Contours from the model velocity field plotted on the velocity residual map. Contours are 338, 340, 345, 350, 355, 260, 365, 370, 372 km s<sup>-1</sup>.

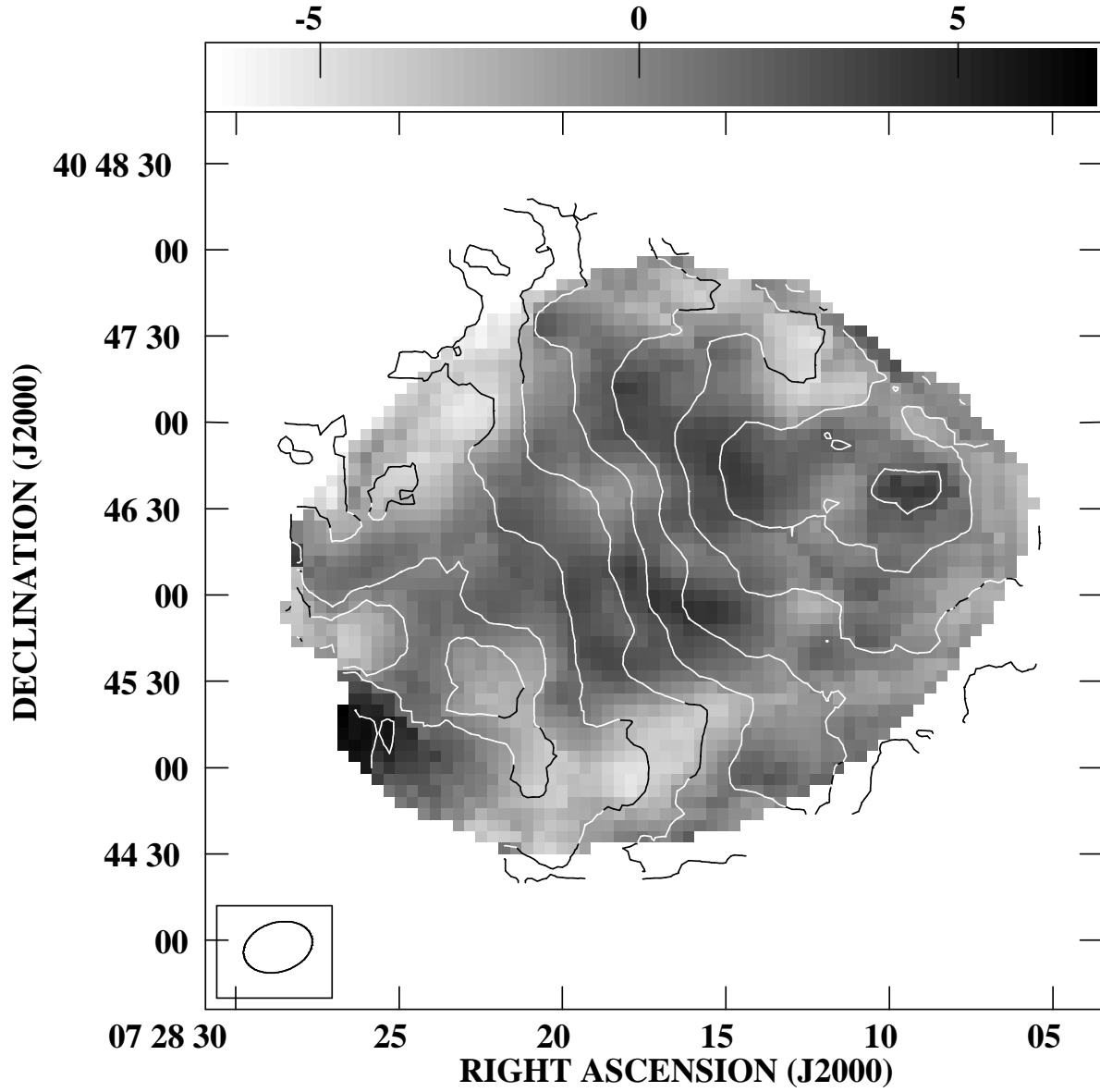


Fig. 18.— The greyscale shows the velocity residual map; contours are from the observed velocity field and are at 338, 340, 345, 350, 355, 360, 365, 370, 374 km s<sup>-1</sup>.

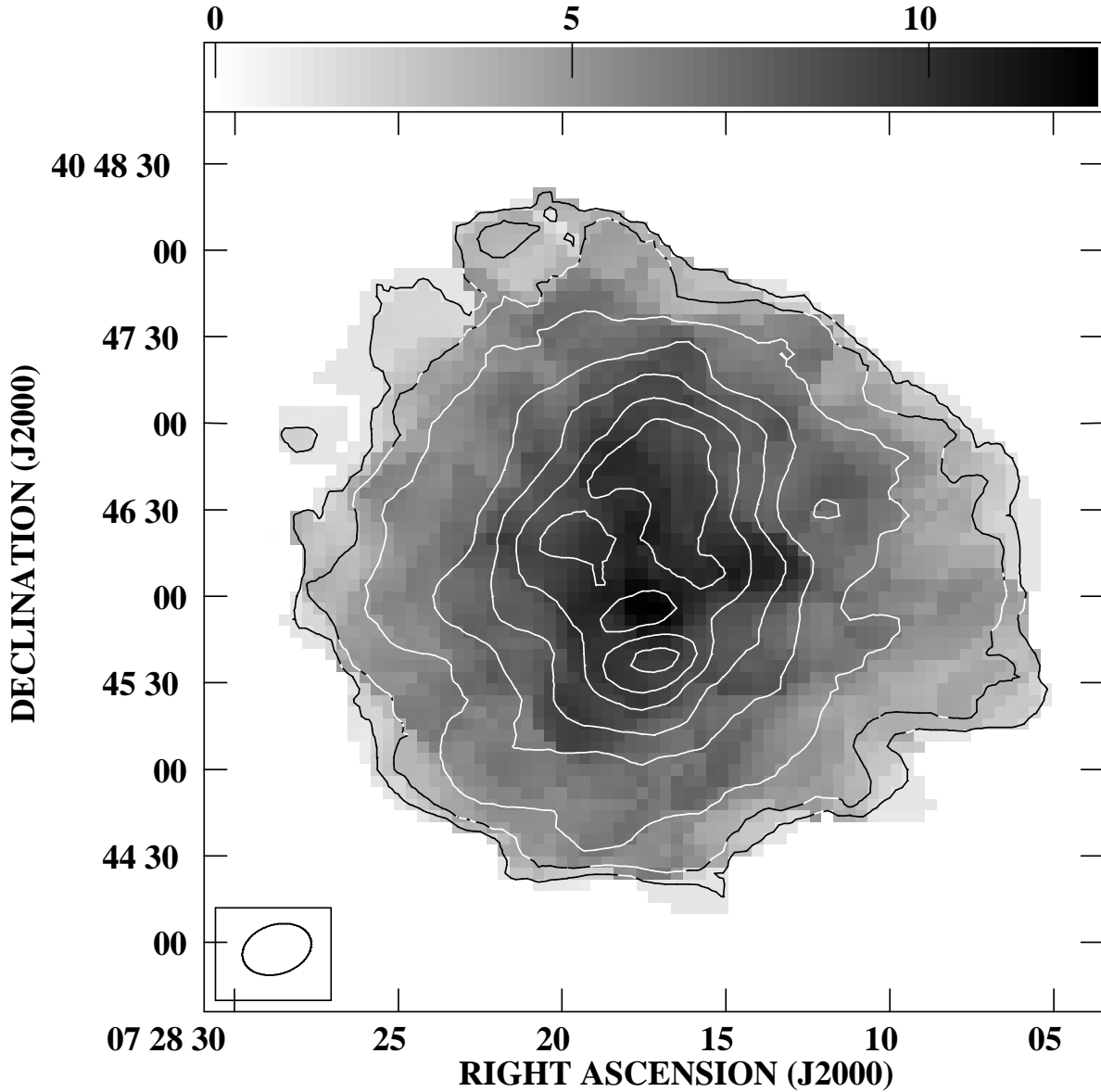


Fig. 19.— The grey-scale shows the velocity dispersion map of DDO 43 made from the  $C+D_{NA}$  cube. Contours are of the integrated HI map: 0.5, 1, 2, 4, 6, 8, 9.5, and  $11 \times 10^{20} \text{ cm}^{-2}$ . The contour in the lower left corner is the FWHM of the beam ( $24.5'' \times 17.1''$ ). The bar code across the top gives the velocity dispersion in  $\text{km s}^{-1}$ .

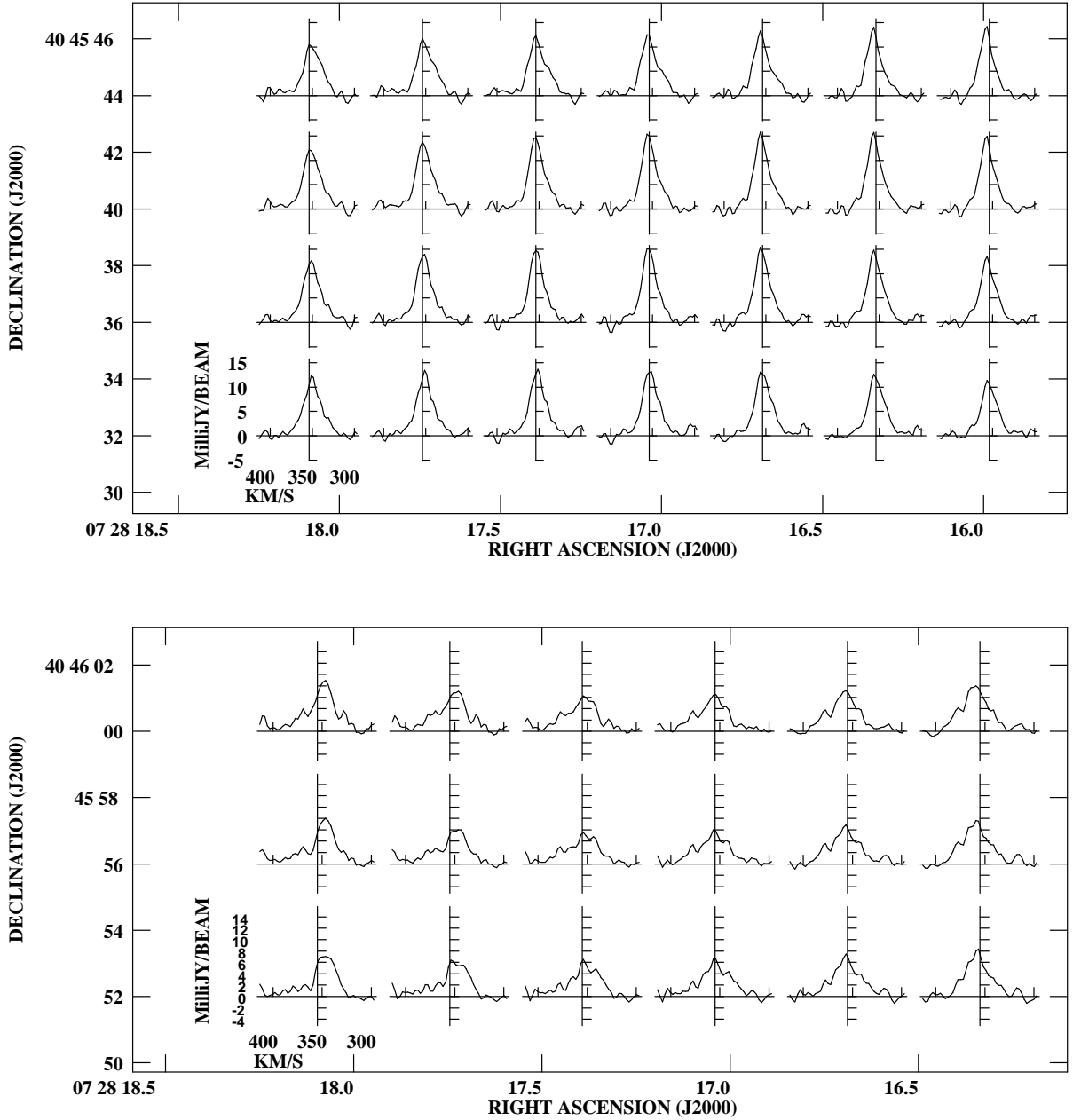


Fig. 20.— Top: Spectra of Knot 1 through the C+D<sub>UN</sub> Hanning-smoothed cube. Each spectrum is from an approximately beam-sized area estimated by averaging 4 pixels together. Bottom: Spectra of Hole 1 through the C+D<sub>UN</sub> Hanning-smoothed cube. Each spectrum is from an approximately beam-sized area estimated by averaging 4 pixels together.



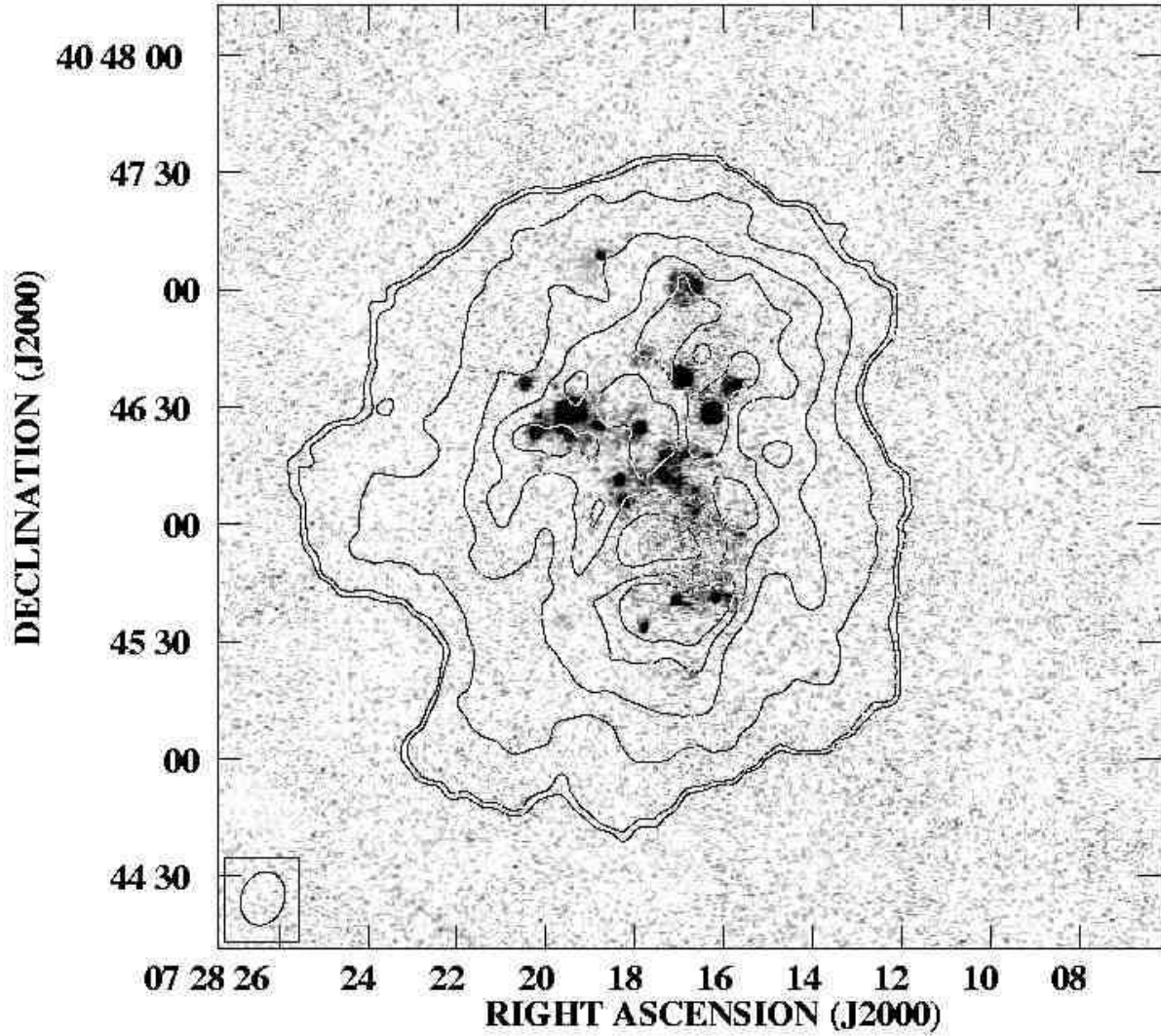


Fig. 21.— Contours of the C-configuration integrated H I map shown superposed on our H $\alpha$  image of DDO 43. The H I contours are 0.5, 1.0, 3.6, 7.2, 10, and  $12 \times 10^{20} \text{ cm}^{-2}$ . The contour in the lower left corner is the FWHM of the beam of the C-configuration H I map:  $14'' \times 11''$ .

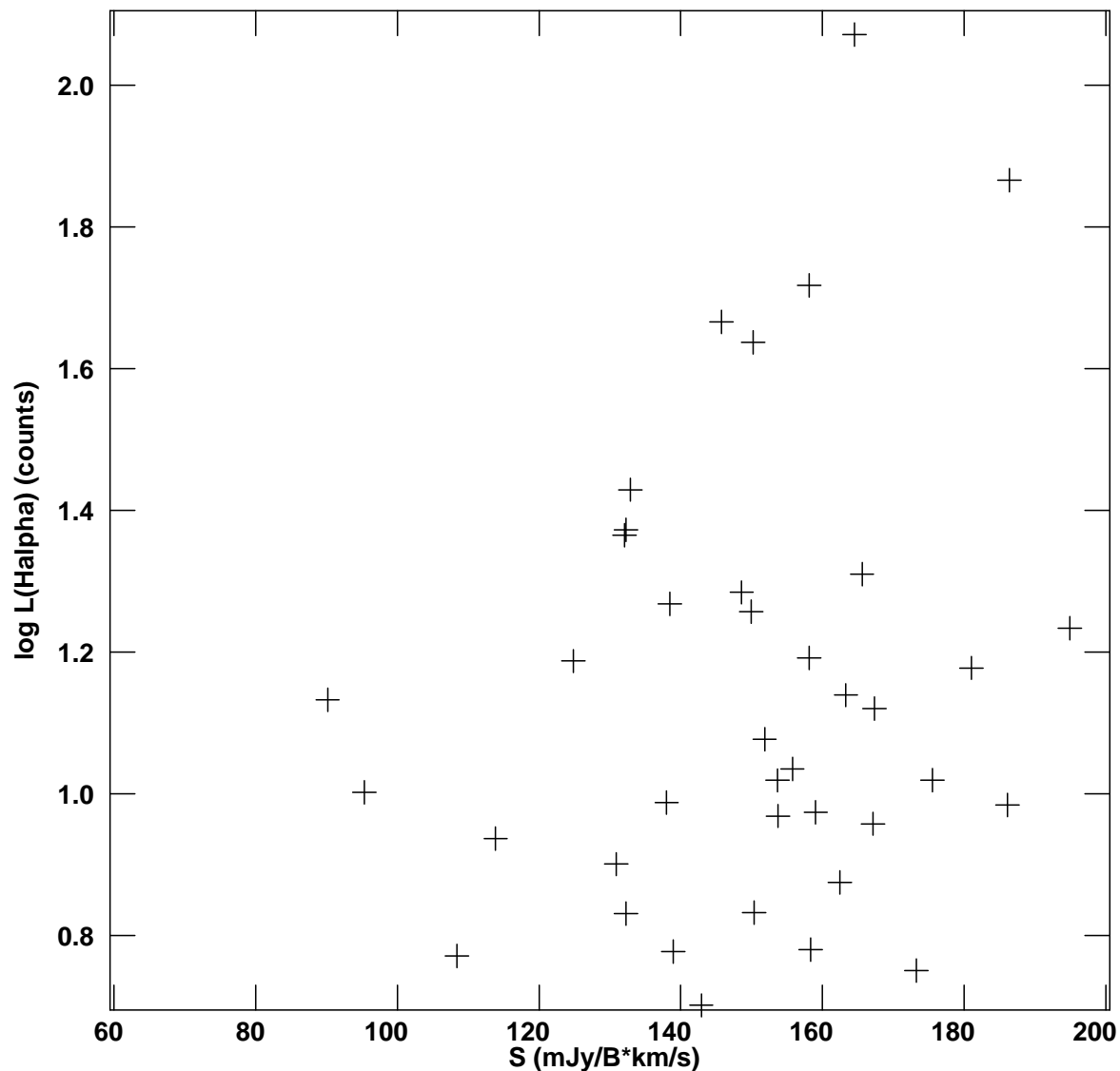


Fig. 22.— Brightnesses of individual pixels are compared in HI and H $\alpha$ . The integrated C-configuration HI map was geometrically matched to the H $\alpha$  image, and then they were both averaged  $20 \times 20$  to produce a pixel scale of  $9.8''$ , close to the beam of the original C-configuration HI map ( $14'' \times 11''$ ). The x-axis is the HI pixel brightness in  $\text{mJy Beam}^{-1} \text{ km s}^{-1}$  where  $60 \text{ mJy Beam}^{-1} \text{ km s}^{-1}$  corresponds to a column density of  $4.3 \times 10^{20} \text{ cm}^{-2}$ . The y-axis is the logarithm of the H $\alpha$  pixel brightness in counts in the image where 1 count corresponds to an H $\alpha$  luminosity of  $1.95 \times 10^{33} \text{ ergs s}^{-1}$ , corrected for reddening.